# Microscopic study of the isoscalar giant resonances in $^{208}$Pb induced by inelastic $\alpha$ scattering

Do Cong Cuong[1], Dao T. Khoa[1] and Gianluca Colò[2]

[1] *Institute for Nuclear Science & Technique, VAEC*
*179 Hoang Quoc Viet Rd., Nghia Do, Hanoi, Vietnam.*
[2] *Dipartimento di Fisica, Università degli Studi di Milano, and INFN, Sez. di Milano*
*via Celoria 16, 20133, Milano, Italy.*

**Abstract**

The energetic beam of (spin and isospin zero) $\alpha$-particles remains a very efficient probe for the nuclear isoscalar giant resonances. In the present work, a microscopic folding model study of the isoscalar giant resonances in $^{208}$Pb induced by inelastic $\alpha$+$^{208}$Pb scattering at $E_{\rm lab} = 240$ and 386 MeV has been performed using the (complex) CDM3Y6 interaction and nuclear transition densities given by both the collective model and Random Phase Approximation (RPA) approach. The fractions of energy weighted sum rule around the main peaks of the isoscalar monopole, dipole and quadrupole giant resonances were probed in the Distorted Wave Born Approximation analysis of inelastic $\alpha$+$^{208}$Pb scattering using the double-folded form factors given by different choices of the nuclear transition densities. The energy distribution of the $E0$, $E1$ and $E2$ strengths given by the multipole decomposition analyses of the $(\alpha, \alpha')$ data under study are compared with those predicted by the RPA calculation.

*Key words:* Inelastic $\alpha$+$^{208}$Pb scattering, isoscalar giant resonances in $^{208}$Pb, folding model analysis

*PACS:* 24.10.Eq, 25.55.Ci, 27.20.+n

## 1. Introduction

Isoscalar giant resonances [1] in medium and heavy nuclei are the pronounced manifestation of nuclear collective motion and, hence, they carry important information about the dynamics of the nuclear excitation process and the properties of the nuclear Hamiltonian. Although their systematic study started more than three decades ago, a number of challenging questions still remain open. For example, the observed compressional modes, like the $L = 0$ isoscalar giant monopole resonance (ISGMR) or the $L = 1$ isoscalar giant dipole resonance (ISGDR), provide the optimal route to determine the nuclear matter incompressibility $K_\infty$, a key quantity specifying the equation of state of nuclear matter. However, the compatibility of the $K_\infty$ values deduced from these two collective compressional modes is still under discussion (see, e.g., Refs. [2, 3] and references therein). The isoscalar giant quadrupole resonance (ISGQR) and the isovector giant dipole resonance (IVGDR) are well known in stable nuclei but it is remains unclear how these two modes evolve in the unstable neutron-rich nuclei.

Since the first observation of ISGMR in $^{208}$Pb in the 70's of the last century [4, 5, 6], this compressional excitation mode of $^{208}$Pb has been investigated in numerous experimental and theoretical studies due to its fundamental importance in the determination of the nuclear matter incompressibility $K_\infty$. Among the experimental tools, the spin and isospin zero $\alpha$-particle remains the best probe for the isoscalar giant resonances with $\Delta S = \Delta T = 0$ and the most pronounced observations of the ISGMR in $^{208}$Pb have been

made so far in the $(\alpha, \alpha')$ experiments, like the recent high-precision measurements of inelastic $\alpha$+$^{208}$Pb scattering at $E_{\rm lab} = 240$ MeV by the Texas A&M University group [7] and 386 MeV by the Osaka group [8, 9]. The exploratory theoretical studies of the isoscalar dipole mode were done in the early 80s by M.N. Harakeh and A.E.L. Dieperink [10], as well as by N. Van Giai and H. Sagawa [11], but the first direct observation of the ISGDR in the $^{208}$Pb$(\alpha, \alpha')$ reaction has been made only years later by Davis *et al.* [12]. Like the ISGMR, the knowledge about the ISGDR is of vital importance for the determination of the nuclear incompressibility $K_\infty$ [2, 3]. Therefore, both the $(\alpha, \alpha')$ experiments at 240 MeV [7] and 386 MeV [8, 9] were aimed at an accurate measurement of the ISGDR strength distribution in $^{208}$Pb. One of the main problems in the experimental study of giant resonances has been, and still is, the difficulty to disentangle different modes when their energies overlap. For example, the excitation energy of ISGMR in $^{208}$Pb has been accurately determined from the most forward part of the $(\alpha, \alpha')$ cross section measured at 240 MeV to be $E_0 \approx 13.96 \pm 0.20$ MeV [7] while the $(\alpha, \alpha')$ experiment at 386 MeV has deduced $E_0 \approx 13.4 \pm 0.2$ MeV [9] using essentially the same method of multipole decomposition analysis (MDA) to disentangle the ISGMR peak from a mixed spectrum of different $(\Delta S = \Delta T = 0)$ excitations including, in particular, the low-energy peak of ISGDR at an excitation energy around 13 MeV [7, 9].

Moreover, there exists a basic problem when experimental results need to be compared with those predicted by a theoretical structure model. It is common, in the theoretical works, to calculate the strength function $S(E)$

associated with a given nuclear transition operator $Q$, that is,

$$S(E) = \sum_{\nu} \delta(E - E_{\nu}) \mid < \nu|Q|0 > |^2, \tag{1}$$

where $\nu$ labels a complete set of final states which can be excited by acting $Q$ upon the ground state $|0>$. In terms of single-particle degrees of freedom, the isoscalar $L$-multipole operator is given by

$$Q_{LM} = \sum_{i=1}^{A} r_i^L Y_{LM}(\hat{r}_i). \tag{2}$$

In the case of the isoscalar monopole and dipole modes one has to replace $r_i^L$ by $r_i^{L+2}$. The predicted strength function (1) is then used to compare with the corresponding experimental strength distribution deduced for the considered $L$-multipole isoscalar excitation. In reality, however, the measured inelastic scattering data are inclusive spectra over a wide energy range which contain the strengths of isoscalar excitations with different multipolarities as well as the contamination by the continuum background. The 'experimental' strength function for a given $L$-multipole excitation depends strongly, therefore, on both the method to exclude continuum background and the MDA to disentangle contribution of a given multipole from the inelastic scattering spectrum. As a result, the comparison between the theoretical and experimental strength functions can be made in many cases only qualitatively.

Nevertheless, a more direct and quantitative comparison between theory and experiment is possible if the nuclear structure information is accurately included into a microscopic description of the inelastic $(\alpha, \alpha')$ scattering cross section measured for a given peak of the resonance energy, within either the distorted-wave Born approximation (DWBA) or coupled-channel formalism

[13]. The well-known portal of this procedure is the double-folding model (DFM) which uses the nuclear ground state and transition densities of the $\alpha$-projectile and target nucleus and an effective nucleon-nucleon ($NN$) interaction to calculate the $\alpha$-nucleus optical potential (OP) and inelastic scattering form factors (FF) of different multipolarities for the DWBA calculation (see, e.g., Ref. [14] and references therein). We note that the single-folding method [15] has been widely used to calculate the $\alpha$-nucleus inelastic scattering FF, using an appropriate $\alpha$-nucleon interaction and nuclear transition densities given by the collective model, for the multipole decomposition analysis of the experimental spectrum within DWBA [7, 8, 9]. In this respect, the DFM calculation of the $\alpha$-nucleus inelastic scattering FF using a realistic effective $NN$ interaction can be used to probe the transition strength extracted from the MDA for a given isoscalar excitation as well as the reliability of different choices for the nuclear transition densities. The latter aspect is quite essential because the collective model transition density has been shown to be reasonable for the collective modes which are, as a rule, concentrated in a limited energy region while other parts of the spectrum could be dominated by pure particle-hole states or states with intermediate character.

We note further that the existing structure models have been substantially improved in recent years and the nuclear linear response theory has been used successfully to describe the excitation of vibrational modes. In a magic nucleus like $^{208}$Pb where the pairing does not manifest itself, this linear response approach is also known as Random Phase Approximation (RPA) method. RPA has been formulated many years ago, but only recently the

fully selfconsistent calculations without crude approximations have become available. Therefore, it is also timely to study the inelastic $\alpha$-nucleus scattering data measured recently for the known isoscalar modes to see how the RPA nuclear wave functions can be probed in the folding + DWBA analysis of these data. To this goal, we have performed in the present work a detailed folding model analysis of the high-precision inelastic $\alpha$+$^{208}$Pb scattering data measured at $E_{\rm lab} = 240$ MeV [7] and 386 MeV [8, 9], using a *complex* version of the density dependent CDM3Y6 interaction [16] and nuclear transition densities given by both the collective model (CM) and the RPA calculation. After a brief overview of the theoretical formalism in Sec. 2, results of the DFM + DWBA analysis of the considered $(\alpha, \alpha')$ data using the CM transition densities are presented and discussed in Sec. 3. The RPA description of the $E0$, $E1$ and $E2$ strength distributions and DFM + DWBA results given by the RPA transition densities are discussed in Sec. 4. The main conclusions and perspectives are given in the Summary.

## 2. Formalism

In this Section, we briefly describe the theoretical model used to calculate the inelastic $(\alpha, \alpha')$ cross sections in the DWBA. As mentioned above, our microscopic study of the inelastic $\alpha$+$^{208}$Pb scattering is based on the double-folding model [14] which uses the nuclear ground state and transition densities of the $\alpha$-projectile and target nucleus and an appropriate effective $NN$ interaction to calculate the $\alpha$-nucleus OP and inelastic scattering FF for the DWBA analysis. The nuclear structure information on the isoscalar giant resonances in $^{208}$Pb is embedded in the nuclear transition densities used

in the folding calculation of the inelastic scattering FF. Two choices of the nuclear transition densities were used in the present work: the phenomenological transition densities given by the collective model (discussed below in Sec. 2.3) and microscopic transition densities given by the RPA approach (discussed in Sec. 2.4).

### *2.1. Effective density dependent NN interaction*

Among various choices of the effective $NN$ interaction, a density dependent version of the M3Y interaction (dubbed as CDM3Y6 interaction [16]) has been used successfully in the folding model analyses of the (refractive) elastic and inelastic $\alpha$-nucleus scattering (see the recent review in Ref. [17]). The density dependent parameters of the CDM3Y6 interaction were carefully adjusted in the Hartree-Fock (HF) scheme to reproduce the saturation properties of nuclear matter [16]. The first version of the CDM3Y6 interaction is *real* and can be used to predict the real OP and inelastic scattering FF only. To avoid a phenomenological choice of the imaginary OP and inelastic scattering FF, we have supplemented the real CDM3Y6 interaction with a realistic *imaginary* density dependence whose parameters were determined based on the Brueckner Hartree-Fock (BHF) results for the nucleon OP in nuclear matter by Jeukenne, Lejeune and Mahaux (JLM) [18]. It has been shown in our recent work [19] that the same form of the CDM3Y functional [16] can be used to obtain the density dependence of the *imaginary* term. Thus, the complex CDM3Y6 interaction used in the present folding model analysis is determined as

$$\text{Re(Im)}\ v_{\text{D(EX)}}(E,\rho,s) = F_{\text{R(I)}}(E,\rho)v_{\text{D(EX)}}(s), \tag{3}$$

$$F_x(E,\rho) = C_x[1 + \alpha_x \exp(-\beta_x \rho) - \gamma_x \rho],\ x = \mathrm{R}, \mathrm{I}. \tag{4}$$

The radial parts of the direct and exchange interactions $v_{\mathrm{D(EX)}}(s)$ were kept unchanged, as derived [14] from the M3Y interaction based on the G-matrix elements of the Paris $NN$ interaction [20], in terms of three Yukawas

$$\begin{aligned} v_{\mathrm{D}}(s) &= 11061.625\frac{\exp(-4s)}{4s} - 2537.5\frac{\exp(-2.5s)}{2.5s}, \\ v_{\mathrm{EX}}(s) &= -1524.25\frac{\exp(-4s)}{4s} - 518.75\frac{\exp(-2.5s)}{2.5s} - 7.8474\frac{\exp(-0.7072s)}{0.7072s}. \end{aligned} \tag{5}$$

While parameters of the real density dependence $F_{\mathrm{R}}$ were taken from the original HF calculation of nuclear matter [16], those of the imaginary density dependence $F_{\mathrm{I}}$ were adjusted iteratively until the HF result for the imaginary nucleon OP in nuclear matter agrees reasonably with the JLM result [18] as well as the shape of imaginary folded OP becomes close to the phenomenological Woods-Saxon imaginary OP found at each energy. All parameters of the complex density dependence are given in Table 1. We note that the dynamic change in the density dependence $F_x(\rho)$ caused by the excitation of the target is taken into account properly in the folding calculation using method given in Ref. [14].

*2.2. Double-folding model*

The generalized double-folding model of Ref. [14] was used to evaluate the complex $\alpha$-nucleus OP and inelastic scattering FF from the following HF-type matrix elements of the CDM3Y6 interaction (3)-(4) between the projectile nucleon $i$ and target nucleon $j$

$$U_{A\to A^*} = \sum_{i\in\alpha; j\in A, j'\in A^*} [< ij'|v_{\mathrm{D}}|ij > + < ij'|v_{\mathrm{EX}}|ji >], \tag{6}$$

where $A$ and $A^*$ are states of the target in the entrance- and exit channel of the $\alpha$-nucleus scattering, respectively. Thus, Eq. (6) gives the (diagonal) elastic OP if $A^* = A$ and (nondiagonal) inelastic scattering FF if otherwise. The (local) direct term is readily evaluated by the standard double-folding integration

$$U_{\rm D}(E, \boldsymbol{R}) = \int \rho_\alpha(\boldsymbol{r}_\alpha)\rho_A(\boldsymbol{r}_A)v_{\rm D}(E, \rho, s)d^3r_\alpha d^3r_A, \\ \boldsymbol{s} = \boldsymbol{r}_A - \boldsymbol{r}_\alpha + \boldsymbol{R}. \tag{7}$$

The antisymmetrization gives rise to the exchange term in Eq. (6) which is, in general, nonlocal in the coordinate space. However, it has been shown [14, 17] that an accurate local equivalent exchange potential can be obtained using the local WKB approximation [13] for the change in relative motion induced by the exchange of spatial coordinates of each interacting nucleon pair

$$U_{\rm EX}(E, \boldsymbol{R}) = \int \rho_\alpha(\boldsymbol{r}_\alpha, \boldsymbol{r}_\alpha + \boldsymbol{s})\rho_A(\boldsymbol{r}_A, \boldsymbol{r}_A - \boldsymbol{s})v_{\rm EX}(E, \rho, s) \\ \times \exp\left(\frac{i\boldsymbol{K}(\boldsymbol{R})\boldsymbol{s}}{M}\right) d^3r_\alpha d^3r_A. \tag{8}$$

Here $\boldsymbol{K}(\boldsymbol{R})$ is the local momentum of relative motion determined from

$$K^2(\boldsymbol{R}) = \frac{2\mu}{\hbar^2}[E_{\rm c.m.} - {\rm Re}\ U_0(E, \boldsymbol{R}) - V_C(\boldsymbol{R})], \tag{9}$$

where $\mu$ is the reduced mass, $M = 4A/(4+A)$, $E_{\rm c.m.}$ is the scattering energy in the center-of-mass (c.m.) frame, $U_0(E, \boldsymbol{R})$ and $V_C(\boldsymbol{R})$ are the nuclear and Coulomb parts of the *real* $\alpha$-nucleus OP, respectively. The calculation of $U_{\rm D(EX)}$ is done iteratively based on a density-matrix expansion method [14, 23]. All technical details of the folding calculation of $U_{\rm D(EX)}$ are the same

as those given in Ref. [14], excepting the use of a realistic local approximation for the *transition* density matrix suggested by Love [24] and a recoil correction to the exchange term (8) suggested by Carstoiu and Lassaut [25].

*2.3. Collective model for the nuclear transition densities*

To calculate consistently both the OP and inelastic scattering FF for the $\alpha$+$^{208}$Pb system one needs to represent the target density in terms of the ground state (g.s.) and transition parts as $\rho(\boldsymbol{r}) = \rho_0(r) + \delta\rho(\boldsymbol{r})$. The explicit expression of the inelastic scattering FF for a given isoscalar excitation (see Ref. [14]) can be deduced from the double-folding integrals (7)-(8), using the following multipole decomposition of $\delta\rho(\boldsymbol{r})$

$$\delta\rho(\boldsymbol{r}) = \sum_{LM} C_L \delta\rho_L(r)[i^L Y_{LM}(\hat{\boldsymbol{r}})]^*, \tag{10}$$

where $C_0 = \sqrt{4\pi}$ and $C_L$=1 for $L \neq 0$. Given the strong collective nature of the isoscalar giant resonances, macroscopic methods to construct the nuclear transition density of the $2^L$-pole isoscalar excitation $\delta\rho_L(r)$, based on the collective model, are widely used in the folding model calculation [15, 26] and multipole decomposition analysis [5, 6, 7, 8, 9] of the $(\alpha, \alpha')$ data.

For the isoscalar giant resonances with $L \geq 2$, we adopt the so-called Bohr-Mottelson prescription [27] to construct the transition densities

$$\delta\rho_L(r) = -\delta_L \frac{d\rho_0(r)}{dr}. \tag{11}$$

Here $\rho_0(r)$ is the g.s. density and $\delta_L$ is the deformation length of the considered isoscalar excitation. The g.s. density of $^{208}$Pb was taken as a Fermi distribution with parameters [28] chosen to reproduce the shell-model density for $^{208}$Pb. Within the *isoscalar* assumption [14, 26] the same deformation

length $\delta_L$ is employed, as a rule, for both the neutron and proton parts of the nuclear transition density (11). For the low-lying excitations, like the first $3^-$ state in $^{208}$Pb considered below, the deformation length is normally determined [14] from the measured electric transition strength $B(EL)$. In terms of the energy weighted sum rule (EWSR) for the operator (2), if a single state $|\nu>$ at the excitation energy $E_\nu$ exhausts 100% of the isoscalar EWSR then the corresponding deformation length is determined [26] as

$$\delta_L^2(E_\nu) = \frac{\hbar^2}{2m}\frac{4\pi}{AE_\nu}\frac{L(2L+1)^2}{(L+2)^2}\frac{< r^{2L-2} >}{< r^{L-1} >^2}; \; < r^{L-1} >= \frac{\int \rho_0(r) r^{L+1} dr}{\int \rho_0(r) r^2 dr}. \quad (12)$$

In the case of ISGMR, the pure breathing mode (or scaling) assumption [29] is used to construct the nuclear transition density

$$\delta\rho_0(r) = -\delta_0 \left[ 3\rho_0(r) + r\frac{d\rho_0(r)}{dr} \right]. \quad (13)$$

If an isoscalar monopole state $|\nu>$ at the excitation energy $E_\nu$ exhausts 100% of the monopole EWSR then its deformation length is determined [26] as

$$\delta_0^2(E_\nu) = \frac{\hbar^2}{2m}\frac{4\pi}{AE_\nu}\frac{1}{< r^2 >}. \quad (14)$$

Another special case is that of the isoscalar dipole excitation for which a macroscopic model based on the compressional hypothesis, with a proper center-of-mass subtraction, has been suggested by Harakeh and Dieperink [10]. Dropping the high-order term $\epsilon$ which is negligible for $A \geq 20$ [10], the transition density of an isoscalar dipole state is written as

$$\delta\rho_1(r) = -\frac{\delta_1}{R}\left[ 3r^2\frac{d}{dr} + 10r - \frac{5}{3} < r^2 > \frac{d}{dr} \right] \rho_0(r), \quad (15)$$

where $R$ is the half-density radius of the g.s. density distribution $\rho_0(r)$. If an isoscalar dipole state $|\nu>$ at the excitation energy $E_\nu$ exhausts 100% of

the EWSR for the dipole operator, with spurious c.m. oscillation subtracted [10, 11], then its deformation length is

$$\delta_1^2(E_\nu) = \frac{6\pi\hbar^2}{mAE_\nu} R^2 \left[ 11 < r^4 > - \frac{25}{3} < r^2 >^2 \right]^{-1}. \qquad (16)$$

The CM transition densities (11)-(16) are normalized in our calculation to describe the excitation process $|\text{g.s.} > \rightarrow |\nu >$, that is, they correspond to the upward transition amplitude. In this way, the corresponding isoscalar transition strength is $S_L = |M_L|^2$ with the transition moment determined as

$$\begin{aligned} M_L &= \int dr\ r^{L+2} \delta\rho_L(r) \qquad \text{if} \quad L \geq 2, \\ M_L &= \int dr\ r^4 \delta\rho_L(r) \qquad \text{if} \quad L = 0, \\ M_L &= \int dr \left( r^3 - \frac{5}{3} < r^2 > r \right) r^2 \delta\rho_L(r) \qquad \text{if} \quad L = 1. \end{aligned} \qquad (17)$$

*2.4. Microscopic RPA transition densities*

Despite a certain success of the collective model transition densities in numerous folding model studies of the isoscalar giant resonances induced by inelastic $\alpha$-nucleus scattering, there is no firm experimental evidence validating their use. In the case of ISGMR, for example, there are only some results of structure calculations showing that (13) is a good representation of the ISGMR transition density in the surface region [30]. Moreover, the radial shapes of the collective model transition densities are assumed to be independent of the excitation energies, which is surely not the case in the reality. Therefore, the folding model analysis based on the transition densities (for a given isoscalar mode) calculated selfconsistently at different excitation energies by a microscopic RPA or quasiparticle RPA (QRPA) approach is

expected to provide a complementary and useful insight. While the QRPA transition densities have been shown to give reasonably good results in many cases like, e.g., in the folding model study of the lowest $2^+$ states in the Sulfur isotopes induced by inelastic proton scattering [31], QRPA or RPA do not systematically provide good results for the low-lying isoscalar excitations when strong anharmonic effects are present. In this sense, RPA is expected to be more suitable for giant resonances and it is, therefore, of interest to probe the RPA transition densities in the present study. We note in this context a similar attempt done recently to study the charge exchange ($^3$He,$t$) reaction [32]. In general, the full coupling between the microscopic structure and reaction models should be, in our opinion, pursued more extensively.

In the present calculations, we have chosen the parametrization set SLy5 [33] of the Skyrme interaction for the RPA calculation of the isoscalar states in $^{208}$Pb. We first solve the HF equations in the coordinate space to construct the single-particle basis. All the radial integrals are computed up to a maximum radius of 22.5 fm, using a mesh of 0.15 fm. The unoccupied single-particle states, including those at positive energies, are obtained by putting the system in a large box of 22.5 fm, that is, the continuum is discretized. A basis of particle-hole ($ph$) configurations is then built upon all occupied states, as well as the lowest unoccupied states with increasing values of the principal quantum number $n$, for each allowed value of $(l, j)$. The RPA matrix equations are then solved in this basis, which has been checked to be large enough to ensure that the appropriate sum rules are satisfied. The procedure has already been explained in Ref. [34].

From the solutions of the RPA equations, the energies $E_\nu$ of the excited

states $|\nu>$ as well as their wave functions are readily obtained. The radial transition density $\delta\rho_{L\nu}(r)$ associated with a given ($2^L$-pole) RPA state $|\nu>$ is given by

$$\delta\rho^{(q)}_{L\nu}(r) = \sum_{ph\in q} \left( X^{(L\nu)}_{ph} + Y^{(L\nu)}_{ph} \right) < p||Y_L||h > R_p(r)R_h(r), \qquad (18)$$

where $X$ and $Y$ are the forward and backward RPA amplitudes and $R(r)$ labels the radial part of the single-particle wave function. The proton and neutron parts (labelled by $q = p, n$) of the transition density (18) are computed separately. The isoscalar transition strength of the RPA state $|\nu>$ is evaluated as $S_{L\nu} = |M_{L\nu}|^2$, where the transition moment $M_{L\nu}$ is

$$M_{L\nu} = \int dr\ r^{L+2} \left[ \delta\rho^{(p)}_{L\nu}(r) + \delta\rho^{(n)}_{L\nu}(r) \right] \qquad \text{if} \quad L \geq 2,$$

$$M_{L\nu} = \int dr\ r^{4} \left[ \delta\rho^{(p)}_{L\nu}(r) + \delta\rho^{(n)}_{L\nu}(r) \right] \qquad \text{if} \quad L = 0,$$

$$M_{L\nu} = \int dr \left( r^3 - \frac{5}{3} < r^2 > r \right) r^2 \left[ \delta\rho^{(p)}_{L\nu}(r) + \delta\rho^{(n)}_{L\nu}(r) \right] \qquad \text{if} \quad L = 1 \qquad (19)$$

## 3. Double-folding model + DWBA analysis using the collective model transition densities

To generate realistic distorted waves for the DFM + DWBA study of the isoscalar giant resonances, we first used the nuclear g.s. densities of $^4$He and $^{208}$Pb taken from Refs. [35] and [28], respectively, to calculate the complex folded OP for the optical model (OM) analysis of the elastic $\alpha$+$^{208}$Pb scattering data at $E_{\rm lab} = 240$ MeV [7] and 386 MeV [8]. To fine tune the complex strength of the CDM3Y6 interaction (3), renormalization coefficients $N_{\rm R}$ and $N_{\rm I}$ of the real and imaginary elastic folded potentials (6) were adjusted by the OM fit to the elastic data at each energy (see OM results shown in upper

panel of Fig. 1). One can see from Table 1 that the best-fit $N_{\rm R}$ coefficient is rather close to unity. The best-fit $N_{\rm I}$ of about 1.4 is reasonable because the imaginary strength of the CDM3Y6 interaction was tuned to the BHF results for nuclear matter and gives, therefore, only the "volume" absorption. To effectively account for the surface absorption caused by inelastic scattering and transfer reactions, an enhanced $N_{\rm I}$ coefficient is naturally needed (compare the dash and solid curves in upper part of Fig. 1). Our OM calculation also predicted the total reaction cross sections $\sigma_{\rm R}$ very close to the experimental values measured at the nearby energies. Thus, the elastic distorted waves given by the present DFM calculation should be accurate for the DWBA analysis of inelastic $\alpha$+$^{208}$Pb scattering.

For the inelastic scattering form factor, a standard method used so far in the DFM + DWBA analyses of inelastic $\alpha$-nucleus scattering [14, 15] is to scale the real and imaginary inelastic folded FF by the same renormalization coefficients $N_{\rm R}$ and $N_{\rm I}$ as those deduced from OM analysis of elastic scattering data. We show in lower panel of Fig. 1, as illustration, the DWBA description of inelastic $\alpha$+$^{208}$Pb scattering data for $3^-_1$ state of $^{208}$Pb given by the inelastic folded FF scaled by the same coefficients $N_{\rm R}$ and $N_{\rm I}$ as those given in Table 1. By using a deformation length $\delta_L$ of the CM transition density (11) chosen to reproduce the measured transition rate $B_{\rm exp}(E3) \approx 611 \times 10^3\ e^2\ {\rm fm}^6$ [36], a very satisfactory description of the inelastic scattering data for $3^-_1$ state of $^{208}$Pb has been obtained. About the same good DWBA description was also obtained with the microscopic nuclear transition density (18) given by the RPA calculation, without any *ad hoc* adjustment. We note that the Coulomb part of inelastic scattering FF is obtained in the present work by

double folding the proton parts of the $^4$He g.s. density and $^{208}$Pb transition density with the Coulomb interaction, using a folding method similar to that used for the nuclear part.

*3.1. MDA and deformation lengths for the CM transition densities*

Before discussing the DFM + DWBA results for the isoscalar giant resonances we briefly recall here how the experimental transition strengths are determined from the multipole decomposition analysis of the measured $(\alpha, \alpha')$ angular distributions [7, 8, 9]. At a given energy bin, the measured (double) differential cross section is expressed within the MDA as a superposition of the angular distributions calculated for different transferred angular momenta $L$ as

$$\left[\frac{d^2\sigma}{d\Omega dE}(\Theta_{\rm c.m.}, E_x)\right]^{\rm exp.} = \sum_{L=0}^{L_{\rm max}} a_L(E_x) \left[\frac{d^2\sigma}{d\Omega dE}(\Theta_{\rm c.m.}, E_x)\right]_L^{\rm calc.} . \qquad (20)$$

Here $[d^2\sigma/d\Omega dE]_L^{\rm calc.}$ is calculated within the DWBA using the inelastic scattering FF generated from the appropriate CM nuclear transition density (11)-(16) by a single-folding method [15]. The CM nuclear transition densities entering the MDA are first determined with 100% exhaustion of the corresponding EWSR (see Sec. 2.3), then a least-$\chi^2$-fit procedure determines all $a_L(E_x)$ coefficients for the considered experimental energy bin. As a result, each best-fit $a_L(E_x)$ coefficient represents the fraction of EWSR exhausted by the corresponding isoscalar $2^L$-pole excitation mode in the energy bin under the MDA analysis. In terms of deformation length $\delta_L$ for a given excitation mode in the considered energy bin $a_L(E_x) = (\delta_L/\delta_L^{\rm max})^2$, where $\delta_L^{\rm max}$ is the maximum deformation length determined [see Eqs. (12), (14) and (16)] to exhaust 100% of the corresponding EWSR.

The MDA analysis of the inelastic $\alpha$+$^{208}$Pb scattering data at $E_{\rm lab} = 240$ MeV measured by the Texas A&M University group [7] was done in the energy bins of 640 or 800 keV width to deduce the isoscalar $EL$ strength distributions over a wide range of excitation energy. The MDA of the 240 MeV data shows, in particular, that the full exhaustion (around 100%) of the isoscalar EWSR has been observed for the ISGMR and ISGQR. The main ISGMR peak has been accurately determined from the 240 MeV data to be at $E_x \approx 13.96 \pm 0.20$ MeV with a width $\Gamma \approx 2.88 \pm 0.20$ MeV, and fragmentation of the $E0$ strength up to about 20 MeV has been observed. The MDA analysis of high-precision inelastic $\alpha$+$^{208}$Pb scattering data measured by the Osaka group at $E_{\rm lab} = 386$ MeV [8, 9] (done in the energy bins of 1 MeV width) has shown a much stronger fragmentation of the $E0$ strength over excitation energies well above 30 MeV, and a less pronounced ISGMR peak (observed at $E_x \approx 13.4 \pm 0.2$ MeV with a wider width $\Gamma \approx 4.0 \pm 0.4$ MeV).

One could reproduce the ISGMR peaks observed in the $(\alpha, \alpha')$ experiment at 240 MeV [7] and 386 MeV [8, 9] in the microscopic structure models, using either nonrelativistic or relativistic functionals which give $K_\infty \approx 240 \pm 20$ MeV [37, 38]. This is why some consensus has been reached [2, 3] on this empirical value for $K_\infty$, where the error of $\pm$ 20 MeV is not simply associated with the experimental uncertainty on the ISGMR energy, but rather with our still incomplete understanding of the structure of energy functionals (in particular, of their density dependence). In this connection, we note that a pure *experimental* discrepancy of 500 keV in the observed ISGMR peaks could also result in a difference of $\Delta K_\infty \approx 20$ MeV in the $K_\infty$ values extracted from empirical formulas relating the ISGMR peak in $^{208}$Pb and nuclear matter

incompressibility $K_\infty$ [3, 40, 41]. Such a difference is quite sizeable and hinders any further theoretical modelling of the energy functionals.

If one uses a microscopic structure approach to determine $K_\infty$ from the ISGMR data, the location of $E_{\rm ISGMR}$ will affect the deduced $K_\infty$ value. In about the same way, the observed ISGDR peak may also be directly related to the $K_\infty$ value [1, 2, 3]. Given such a vital importance of the ISGMR and ISGDR excitations in determining the nuclear matter incompressibility $K_\infty$ and the fact that a simple single-folding method [15] was used to calculate the $\alpha$+$^{208}$Pb inelastic scattering FF for the MDA analyses of Refs. [7, 8, 9], we deem it necessary to probe the ISGMR and ISGDR strength distributions extracted from these two experiments again in our DFM + DWBA approach.

It is complementary to note that the density dependent CDM3Y6 interaction used in the present DFM calculation was parametrized in the HF scheme to reproduce $K_\infty = 252$ MeV at the saturation density of symmetric nuclear matter [16, 17], and it has been successfully used in numerous OM and DWBA analyses of elastic and inelastic $\alpha$-nucleus scattering. The isoscalar $EL$ strengths (in terms of exhausted fractions of the corresponding EWSR for $L = 0, 1, 2, 3$) given by the MDA analyses of Refs. [7, 8, 9] for the main peaks of the ISGMR, ISGQR and ISGDR together with those predicted by the RPA calculation are presented in Table 2. Each energy bin in Table 2 has been chosen so that the strongest $EL$ strengths around the main resonance peaks deduced from the two experiments can be used consistently in the same DFM + DWBA calculation. For example, the ISGMR peak was found by the MDA of 240 MeV data [7] and 386 MeV data [8, 9] in the energy bins centered at $E_x \approx 14.1$ and 13.5 MeV, respectively, and the

corresponding $E0$ strengths should be studied in the same DFM + DWBA analysis. The full energy distributions of the $EL$ strengths for $L = 0, 1, 2$ are shown below in Sect. 4.

*3.2. Isoscalar EL strengths near the ISGMR peak*

In Fig. 2 the inelastic $\alpha$+$^{208}$Pb scattering cross section at $E_{\rm lab} = 240$ MeV measured for the 640 keV-wide energy bin centered at $E_x = 14.1$ MeV [7] are compared with the DFM + DWBA results given by the collective model transition density (13)-(14). In this energy bin, the $E0$ strength deduced from the 240 MeV data is strongest and exhausts about 37.6% of the $E0$ EWSR. The isoscalar $E1$ strength is quite significant (6.3% of the $E1$ EWSR) in this energy bin due to the dipole strength coming from the low-energy peak of ISGDR located around 13 MeV and affecting significantly the total angular distribution. The isoscalar $E2$ strength of about 6.6% of the $E2$ EWSR as well as no contribution from isoscalar $E3$ excitation were found in this energy bin [7]. One can see in the lower panel of Fig. 2 that the measured inelastic scattering cross section is reasonably described by the DFM + DWBA calculation using the CM transition densities scaled to the isoscalar ($L = 0, 1, 2$) strengths given by the MDA of Ref. [7]. Given the monopole and dipole angular distributions oscillating out of phase, a smooth angular distribution seen in the 240 MeV data shows clearly the mixture of the $E1$ strength from the low-energy peak of ISGDR in the considered energy bin. Since the MDA of the Osaka data [8, 9] has given the strongest $E0$ strength in the 1 MeV energy bin centered at $E_x = 13.5$ MeV, we found it appropriate to use the isoscalar $EL$ strengths deduced for this energy bin to construct the CM transition densities for our DFM + DWBA analysis of

the 240 MeV data for $E_x = 14.1$ MeV. According to the MDA of the Osaka data, the $E0$ strength is strongly fragmented over a wide energy range and only about 16% of the $E0$ EWSR has been located in the energy bin around the ISGMR peak at $E_x = 13.5$ MeV. While the isoscalar dipole strength deduced from the 386 MeV data is quite close to that deduced from the 240 MeV data, the isoscalar $E2$ strength was found [8, 9] much stronger (up to 15% of the $E2$ EWSR) in the energy bin around $E_x = 13.5$ MeV. On top of that, about 3% of the isoscalar $E3$ EWSR strength was also observed by Uchida *et al.* [8, 9] in this energy bin. The DFM + DWBA description of the 240 MeV data for $E_x = 14.1$ MeV given by the CM transition densities scaled to the isoscalar ($0 \leqslant L \leqslant 3$) strengths taken from Refs. [8, 9] are shown in upper panel of Fig. 2. Although a weaker $E0$ strength deduced by Uchida *et al.* [8, 9] gives a monopole cross section more than 2 times smaller than that obtained with the $E0$ strength deduced by Youngblood *et al.* [7], the overall description of the 240 MeV data given by the isoscalar $EL$ transition strengths taken from Refs. [8, 9] remains satisfactory due to stronger $E2$ and $E3$ contributions. However, the lack of the $E0$ strength can still be seen in the DWBA description of data points at the most forward angles shown in the upper panel of Fig. 2.

It is natural also to check the DFM + DWBA description of the Osaka data at $E_{\rm lab} = 386$ MeV [8, 9, 39] based on the same $EL$ transition strengths as discussed above. In Fig. 3 the inelastic $\alpha$+$^{208}$Pb scattering cross section at $E_{\rm lab} = 386$ MeV measured for the 1 MeV-wide energy bin centered at 13.5 MeV are compared with the DFM + DWBA results given by the CM transition densities (13)-(14) built upon the same isoscalar $EL$

transition strengths as those used in Fig. 2. Except for the two data points at the most forward angles which are fairly described by the $EL$ strengths given by the MDA of the 240 MeV data [7], the present DFM + DWBA results strongly underestimate the measured data over the whole angular range. About the same picture has been found for the energy bin centered at $E_x = 14.5$ MeV when the DFM + DWBA results obtained with the $EL$ strengths deduced for this bin are compared with the inelastic $\alpha$+$^{208}$Pb scattering data at $E_{\rm lab} = 386$ MeV [39]. Such a big gap between the calculated and measured cross sections seen in Fig. 3 is not unexpected because the contributions by the excitation modes of higher multipoles ($L > 3$) are not taken into account in our DFM + DWBA calculation. We recall that the authors of Refs. [8, 9, 39] were able to measured the $(\alpha, \alpha')$ energy spectrum for the lead target without any contamination from the instrumental background by using the high-resolution magnetic spectrometer Grand Raiden, and the MDA analysis of the 386 MeV data has been done for all multipoles up to $L_{\rm max} = 14$ [8, 9, 39]. Since the number of fitting parameters is quite large in this case, it is not excluded that some continuum background coming from other quasi-elastic processes like the pickup/breakup reactions has been simply approximated by the high-multipole terms in the MDA series. Moreover, any strong particle-hole $EL$ excitation with $9 \leqslant L \leqslant 14$ in the energy region around 13-14 MeV would be unlikely from the structure point of view. In contrast to the Osaka experiment, the MDA of the 240 MeV data by the Texas A&M University group was done only after a broad continuum background (presumably caused by the high-multipole $EL$ excitations and pickup/breakup reactions) has been substracted [7]. As a result, the

MDA of the 240 MeV data has been performed with less fitting parameters. The fact that present DFM + DWBA results describe the 240 MeV data reasonably using the $EL$ strengths deduced by the Texas A&M University group [7] seems to indicate that the single-folding method [15] used in their MDA of inelastic $\alpha$-nucleus scattering is quite reliable. However, a closer inspection of the lower part of Fig. 2 and Fig. 5 in Ref. [7] shows that the present DFM + DWBA results are slightly underestimating the data points compared to the MDA results obtained with the single-folding method. To explore such a difference in the case of 386 MeV data, we have compared in Fig. 4 the present DFM + DWBA results with those given by the MDA of the $(\alpha, \alpha')$ data measured for the energy bin centered at $E_x = 14.5$ MeV [8, 9, 39] and found that the DFM + DWBA cross sections are indeed lower than those given by the MDA (with the relative difference in the calculated total cross sections ranging from $\sim 57\%$ at the most forward angles to $\sim 44\%$ at $\Theta_{\rm c.m.} \approx 14^\circ$). In particular, the difference between the DFM + DWBA cross section for $L = 2$ and that given by the MDA is very alarming, as it is $\sim 185\%$ at the most forward angles and $\sim 69\%$ at $\Theta_{\rm c.m.} \approx 14^\circ$ (see dash-dotted curves in Fig. 4). Such a difference is quite significant and can result in sizable differences in the $EL$ transition strengths deduced from the MDA of inelastic $\alpha$-nucleus scattering using either single- or double-folding method. Since the present DFM approach is much more advanced compared to the single-folding method [15] used so far in the MDA, it is not excluded that the $EL$ strengths near the ISGMR or ISGQR peaks deduced from the MDA are somewhat underestimated. In any case, the use of the present DFM approach in the MDA of future $\alpha$-nucleus scattering data is strongly

recommended. We note further that while the ISGMR peaks observed in the two $(\alpha, \alpha')$ measurements seem to be in a reasonable agreement with the existing database [1, 2, 3], the difference in the observed distributions of the isoscalar monopole strength is striking (about a factor of 2 in the most important energy interval). It remains, therefore, an interesting challenge to future experiments to confirm whether the $E0$ strength is mainly localized at the excitation energies below 20 MeV [7] or widely fragmented to energies beyond 30 MeV [8, 9].

### *3.3. Isoscalar EL strengths near the ISGQR peak*

The ISGQR at $E_x \approx 10 \sim 11$ MeV in $^{208}$Pb is perhaps one of the most studied isoscalar giant resonances in nuclei. Nevertheless, like in the case of the ISGMR, the isoscalar $E2$ strength distributions observed in the $(\alpha, \alpha')$ experiments at 240 MeV [7] and 386 MeV [8, 39] are sizeably different. For example, the $E2$ strength has been shown by the MDA of the 240 MeV data to be concentrated mainly near the ISGQR peak and slightly spread over the energies below 21 MeV, exhausting $100 \pm 13\%$ of the $E2$ EWSR [7]. In contrast, the $E2$ strength given by the MDA of the 386 MeV data [8, 39] is broadly spread from about the same ISGQR peak to energies beyond 30 MeV and, hence, exhausts more than 200% of the $E2$ EWSR (based on a direct integration of the tabulated $E2$ strength made available to us by the authors).

In Fig. 5 the inelastic $\alpha$+$^{208}$Pb scattering data at $E_{\rm lab} = 240$ MeV measured for the energy bin centered at $E_x = 10.3$ MeV [7] are compared with the DFM + DWBA predictions based on the $EL$ strengths taken from Refs. [7, 8, 39]. In this energy bin, the $E2$ strength deduced from the 240

MeV data is stronger than that deduced from the 386 MeV data and exhausts about 20% of the $E2$ EWSR, and the DWBA description of the measured angular distribution is better (see lower panel of Fig. 5) if the CM transition densities are scaled to the $EL$ strength deduced from the 240 MeV data [7]. We note that a weak isovector $E1$ strength was also included into the MDA of the 240 MeV data to achieve a better DWBA fit to the data measured for the two energy bins centered at 10.3 and 14.1 MeV [7]. Given a dominant contribution by the isoscalar $EL$ strengths ($0 \leqslant L \leqslant 3$) to the $(\alpha, \alpha')$ cross sections (see lower panels of Figs. 2 and 5), we have chosen not to include the isovector $E1$ mixing into the present DFM + DWBA calculation in order to show explicitly the role of the isoscalar excitation modes. We have also observed (lower panel of Fig. 5) that the present DFM + DWBA results slightly underestimate the data points compared to the MDA results of Ref. [7] and this effect should be due to the use of single-folding method (see further discussion below).

In the energy bin centered at $E_x = 10.9$ MeV for the 240 MeV data (or $E_x = 10.5$ MeV for the 386 MeV data) the $E2$ strengths deduced from both data sets are quite close to each other, exhausting about 19 to 23% of the $E2$ EWSR (see Table 2). In addition, similar $E0$ and $E1$ strengths (from 3 to 4 % of the corresponding EWSR) were also deduced from both experiments. The only difference is a significantly larger $E3$ strength deduced by the MDA of the 240 MeV data for this energy bin. As there is no $(\alpha, \alpha')$ cross section measured at $E_{\rm lab} = 240$ MeV available to us for this energy bin, we compare in Fig. 6 the $(\alpha, \alpha')$ data at $E_{\rm lab} = 386$ MeV measured for the energy bin centered at $E_x = 10.5$ MeV [39] with the DFM + DWBA results given by the

isoscalar $EL$ strengths taken from Refs. [7, 8, 9]. One can see in lower panel of Fig. 6 that the DFM + DWBA results based on the $EL$ strengths taken from the MDA of the 240 MeV data [7] are much closer to the data points compared with similar results for the $(\alpha, \alpha')$ cross sections at $E_{\rm lab} = 386$ MeV shown in lower panels of Figs. 3 and 4. This could well indicate a much weaker contribution by the high multipoles to the $(\alpha, \alpha')$ cross section at the excitation energy around 10 MeV. Like the results obtained above for the excitation energies around 14 MeV, the DFM + DWBA calculation based on the $EL$ strengths taken from the MDA of the 386 MeV data [8, 9] underestimates the data over the whole angular range (see upper panels of Figs. 3, 4 and 6) including the smallest angles where high multipoles are not expected to play a major role.

*3.4. Isoscalar EL strengths near the main ISGDR peak*

The ISGDR in $^{208}$Pb has been observed in both the $(\alpha, \alpha')$ experiments at 240 MeV [7] and 386 MeV [8, 9]. The isoscalar $E1$ strength distribution has been shown clearly by these two experiments to split into two parts: a weak low-energy peak centered at $E_x \approx 13$ MeV and the main, broad high-energy peak at $E_x \approx 22.5$ MeV. In contrast to the ISGMR case, the ISGDR peaks observed in these two measurements are quite close to each other, except for some difference in the width deduced for the low-energy $E1$ peak. Using the empirical formulas [40, 41] relating the high-energy ISGDR peak in $^{208}$Pb and nuclear matter incompressibility $K_\infty$ we obtain $K_\infty \approx 210$ MeV which is smaller than that deduced from the ISGMR data by about 20 MeV.

The inelastic $\alpha$+$^{208}$Pb scattering data at $E_{\rm lab} = 240$ MeV measured for the energy bin centered at $E_x = 22.5$ MeV [7] and DFM + DWBA results

given by the CM transition densities scaled to the isoscalar $EL$ strengths taken from Refs. [7, 8, 39] are shown in Fig. 7. After substraction of the continuum contribution, the MDA [7] implied that the measured $(\alpha, \alpha')$ cross section (see Fig. 7) contains mainly the isoscalar $E1$ and $E3$ components which exhaust, respectively, about 8% and 6% of the corresponding EWSR (see Table 2). The DFM + DWBA calculation based exactly on these $E1$ and $E3$ transition strengths accounts reasonably for the data (lower panel of Fig. 7), with some underestimation of the data points at large angles (due perhaps to the contribution from the isovector $E1$ mode, see Fig. 5 of Ref. [7]). In contrast to the MDA results for the 240 MeV data, in addition to similar isoscalar $E1$ and $E3$ strengths around the peak $E_x = 22.5$ MeV, the MDA of the 386 MeV data [8, 9] has found significant contributions from the isoscalar $E0$ and $E2$ strengths which exhaust, respectively, about 2% and 10% of the corresponding EWSR (Table 2). The DFM + DWBA calculation based on the isoscalar $EL$ strengths given by the MDA of the 386 MeV data also describes reasonably the 240 MeV data for the peak $E_x = 22.5$ MeV (upper panel of Fig. 7). The high-energy tails of the $E0$ and $E2$ strength distributions given by the MDA of the 386 MeV data give rise to an enhancement of the DWBA cross section at the forward angles as shown in upper panel of Fig. 7. In Fig. 8 the 386 MeV data measured for the 1 MeV bin centered at $E_x = 22.5$ MeV are compared with the DFM + DWBA results given by the CM transition densities (13)-(14) based on the same isoscalar $EL$ transition strengths as those used in Fig. 7. Similar to the DFM + DWBA results shown in Figs. 3 and 4, the DFM + DWBA results for the peak $E_x = 22.5$ MeV strongly underestimate the 386 MeV data

over the whole angular range. However, the gap between the calculated and measured cross sections becomes significantly larger in this case which shows the important contributions by the excitation modes of higher multipoles ($L > 3$) at energies above 20 MeV.

Given a sizable difference between the DFM + DWBA results and the MDA results of Ref. [7] found for the energy bin centered at the ISGMR peak shown in Fig. 4, it is necessary to check this effect also for the energy bins centered at the ISGQR and ISGDR peaks. In Fig. 9, the DFM + DWBA results for the $(\alpha, \alpha')$ cross sections at $E_{\rm lab} = 386$ MeV (in the 1-MeV bins centered at $E_x = 10.5$ and 22.5 MeV) are compared with the corresponding MDA results by Uchida *et al.* [8, 9] that are based on the same $EL$ strengths. Although in logarithmic scale these two sets of calculated DWBA cross sections look similar in shape and strength, the MDA cross sections are larger than those given by the DFM + DWBA calculation by about $40 \sim 60\%$ over the whole angular range. For the energy bin centered at the ISGQR peak, this difference is up to $\sim 180\%$ at the most forward angles and is due mainly to the difference in the $E2$ cross sections. Since the Coulomb contribution of the inelastic scattering FF is quite strong at the forward angles for the $E2$ excitation mode, such an unusually large difference in the $E2$ cross sections could be due to the different treatments of the Coulomb inelastic scattering FF in the two approaches. Namely, the Coulomb FF is evaluated in our DFM approach microscopically by double-folding the proton parts of the $^4$He g.s. density and $^{208}$Pb transition density with the Coulomb interaction, with both the direct and exchange terms calculated by a method similar to that used for the nuclear FF, whereas the widely used ansatz for the Coulomb FF in the

MDA of $(\alpha, \alpha')$ data is to assume a simple macroscopic model-independent formula [26] containing the electric transition rate $B(EL)$ of the considered state. To probe this effect, we have made the single-folding calculation [15] of the nuclear FF for these cases, using exactly the same effective $\alpha N$ and CM transition densities as those used in the MDA by Uchida *et al.* [8, 9]. The single-folded nuclear FF were then used with the same microscopic Coulomb FF as that used in the DFM + DWBA calculation to calculate the $(\alpha, \alpha')$ cross sections in the energy bins centered at 10.5 and 22.5 MeV and the results are plotted in Fig. 9 as dash-dotted curves. One can see that the large difference at forward angles in the cross sections given by the single- and double-folding methods is reduced significantly, and at large angles the cross sections given by the single-folded FF are very close to the MDA cross sections. The results shown in Fig. 9 stress again the need to use the accurate DFM in the MDA of the $(\alpha, \alpha')$ data to deduce the realistic $EL$ transition strengths.

In conclusion, the DFM + DWBA analysis of the inelastic $\alpha$+$^{208}$Pb scattering data at $E_{\rm lab} = 240$ MeV measured in the energy bins centered at the peaks of the ISGMR, ISGQR and ISGDR in $^{208}$Pb, using the CM nuclear transition densities for the $EL$ excitation with $L \leqslant 3$, agree qualitatively with the original MDA of these data [7]. Given a sizable difference in the $(\alpha, \alpha')$ cross sections obtained with the single- and double-folding methods for the inelastic scattering FF, the uncertainties in the $EL$ strengths deduced from the MDA of the considered data [7, 8, 9] might be significantly larger. Similar DFM + DWBA analysis of the inelastic $\alpha$+$^{208}$Pb scattering data at $E_{\rm lab} = 386$ MeV strongly underestimates the data points measured in

about the same energy bins and, thus, indicates a strong contribution by the high-multipole ($L > 3$) excitation modes. However, the gap between the calculated and measured cross sections is quite different in the excitation energy regions around 10 MeV and above 20 MeV. This result shows that the maximum angular momentum $L_{\max}$ taken into account in the MDA series (20) seems to be energy dependent if the background due to the high-multipole excitation modes is not explicitly subtracted which is the case for the 386 MeV data [7, 8, 39].

## 4. Results obtained with the microscopic RPA transition densities

Although there is no consensus whether microscopic models like RPA can provide reliable inputs for the nuclear transition densities, it has been shown in the past [31, 42, 43] that for the low-lying excited states of dominating one-phonon structure, the RPA transition densities can be successfully used in the folding model analysis. The DFM + DWBA description of inelastic $\alpha$+$^{208}$Pb scattering data measured for the $3^-_1$ state of $^{208}$Pb given by the RPA nuclear transition density (see lower panel of Fig. 1) is again a convincing example. Of course, there are cases in which RPA is known to have drawbacks, like in the case of low-lying states with a strong *anharmonic* mixture of the two-phonon structure [42]. Isoscalar giant resonances, as already discussed above, should be a good test ground for the RPA wave functions because RPA has been claimed over the years to be a proper theory to describe those resonances. However, these qualitative arguments are often invoked but in fact we are not aware of the conclusive evidences showing that microscopic RPA provides accurate transition densities for inelastic scattering calculations (cf., in this

respect, Refs. [44]). Also, this is probably the first combination of a *fully* self-consistent RPA approach and an advanced microscopic double-folding model, and consequently in the present context the question of the accuracy of the RPA transition densities can be addressed carefully in more detail.

It is impossible to reproduce the full experimental width of a resonance state within the RPA approach. Although the width caused by fragmentation of the resonance strength (the so-called Landau damping) can be accounted for within the RPA, and the escape width can also be accounted for if continuum-RPA is performed, the spreading width (which is by far the most relevant in heavy nuclei) cannot come out from RPA. To have a direct quantitative comparison of the RPA solution with the observed $EL$ strength distribution, we found it necessary to perform some *averaging* [45] of the total RPA strength (19) over the excitation energy $E_x$ as follows

$$\left\langle S_L^{\rm RPA}(E_x)\right\rangle = \sum_\nu S_L^{\rm RPA}(E_\nu) f(E_x - E_\nu), \tag{21}$$

where $\nu$ labels the RPA (isoscalar $EL$) states and a Lorentzian [45] is used as the averaging function $f(E-E')$. In each case, the averaging width $\Delta$ is chosen so that the averaged RPA strength

$$\int_{E_x-0.5\ \rm MeV}^{E_x+0.5\ \rm MeV} \left\langle S_L^{\rm RPA}(E)\right\rangle dE \tag{22}$$

within the 1-MeV energy bin centered at an excitation energy $E_x$ is smooth enough to be compared with that deduced from the MDA analysis of $(\alpha,\alpha')$ data. In the case of ISGMR, a strongly collective resonance RPA state was found at $E_x \approx 14.2$ MeV which is quite close to the experimental ISGMR peak. This RPA state is accompanied by several non-collective RPA states

on either sides of the peak (see upper panel of Fig. 10) and the whole set of monopole RPA states exhausts about 99.5% of the $E0$ EWSR. The averaging width $\Delta \approx 3$ MeV, which is close to the observed ISGMR width [7], was chosen to smooth the strength of the RPA resonance state over the excitation energy. The distribution of *averaged* RPA strength agrees reasonably with those deduced from the MDA analyses of the $(\alpha, \alpha')$ data at 240 MeV [7] and 386 MeV [8, 39] as shown in the lower panel of Fig. 10.

For the ISGQR, most of the microscopic RPA calculations predict a strong $E2$ resonance at somewhat higher excitation energy ($E_x \approx 12.5$ MeV in our case) compared to the experimental ISGQR peak around 10.3 MeV, in keeping with the low effective mass associated with effective Skyrme or Gogny interactions. The lowest $2_1^+$ state is predicted by the RPA at an excitation energy of $E_x \approx 5.1$ MeV which is also higher than the experimental value of about 4.09 MeV. To have comparable $E2$ strengths at the ISGQR peak observed in $(\alpha, \alpha')$ experiment, we have shifted all isoscalar quadrupole RPA states (which exhaust 99.3% of the $E2$ EWSR) down by 2 MeV in the excitation energy and the resulted RPA spectrum is shown in upper panel of Fig. 11. By using the same averaging width $\Delta \approx 3$ MeV which is also close to the observed ISGQR width [7], the distribution of averaged RPA strength agrees well with those deduced from the MDA analyses of the $(\alpha, \alpha')$ data at both energies (see lower panel of Fig. 11). While the averaged RPA strength and that given by the MDA of 240 MeV data [7] are concentrated mainly near the ISGQR peak and slightly spread over $E_x \leq 21$ MeV, the $E2$ strength given by the MDA of 386 MeV data [8, 39] is broadly spread up to much higher excitation energies.

Concerning the ISGDR excitation in $^{208}$Pb, most of the microscopic structure calculations [46, 47, 48] predict the main (high-energy) peak of the ISGDR at $E_x \approx 24.5 \sim 25.5$ MeV which is somewhat higher than that ($E_x \approx 22.5$ MeV) observed in the $(\alpha, \alpha')$ experiments [7, 8, 39]. Like the earlier RPA results obtained with the SLy4 interaction [46], the present RPA calculation using the SLy5 interaction predicts the high-energy peak of the ISGDR at $E_x \approx 25$ MeV. In a similar manner, we have shifted all the isoscalar dipole RPA states (which exhaust 86.5% of the $E1$ EWSR) down by 3 MeV in excitation energy and the shifted spectrum of dipole RPA states is shown in the upper panel of Fig. 12. To have a better resolution of the averaged dipole strength of numerous RPA states found in the resonance region, we have used a finer averaging width of $\Delta \approx 1$ MeV in this case and the distribution of averaged RPA strength agrees reasonably with the observed dipole strength distribution at the main ISGDR peak (see lower panel of Fig. 12). However, as it can be seen in the lower panel of Fig. 12, the low-energy ISGDR strength observed at $E_x \approx 13$ MeV in both $(\alpha, \alpha')$ experiments [7, 8, 39] is not reproduced by the present RPA calculation. Whether this is an experimental or theoretical problem, is an open question. Certainly in most of the microscopic RPA calculations the low-energy ISGDR strength is less collective than the high-energy part (see, e.g., the discussion in Ref. [46]) and, as such, less amenable to a RPA description. Suggestions that this strength corresponds to toroidal motion have been put forward [49] and if this were the case, the capability of microscopic functionals to describe such exotic mode, and the relationship with $(\alpha, \alpha')$ cross sections is even less clear.

Given the energy distributions of the $E0$, $E1$ and $E2$ strengths reasonably

described by the *averaged* RPA strengths as shown above, it is natural to expect that the DFM + DWBA calculation using a proper input of the RPA transition densities should also deliver a good description of the measured $(\alpha, \alpha')$ cross sections. However, to compare the DFM + DWBA results with the $(\alpha, \alpha')$ cross section measured for a given energy bin, one needs to combine properly the transition densities of all RPA states in this energy bin into a total RPA transition density which can be used as input of the DFM calculation. In general, if the number of RPA solutions for a given $EL$ transition in the energy bin $dE$ centered at $E_x$ is $N$, then the total RPA transition density associated with the bin $dE$ should be defined as

$$\delta\rho_L^{\rm RPA}(r) = \sum_{\nu=1}^{N} M_{L\nu}\delta\rho_{L\nu}(r); \text{ with } S_L^{\rm RPA} = \sum_{\nu=1}^{N} S_{L\nu}^{\rm RPA} \equiv \sum_{\nu=1}^{N} |M_{L\nu}|^2. \quad (23)$$

Here $M_{L\nu}$ is the RPA transition moment (19) of the RPA state $|L\nu>$ and $\delta\rho_{L\nu}(r)$ is the corresponding RPA transition density (18). It is natural to choose the transition moment $M_{L\nu}$ as the averaging weight for the RPA transition density $\delta\rho_{L\nu}(r)$, so that the RPA transition density (23) preserves the total transition strength $S_L^{\rm RPA}$ in the considered energy bin as predicted by the RPA calculation. The only question now is whether the total RPA transition density should be scaled to reproduce the averaged RPA strength (22) in this energy bin or should it be kept unchanged as given by the weighted sum (23) of all RPA transition densities. We have found, however, that the first procedure is reasonable only for the transition densities $\delta\rho_{L\nu}(r)$ of the strongest RPA states with $L = 0$ and 2 in the energy bins around the ISGMR and ISGQR peaks, respectively. For the RPA states of other multipolarities $(L = 1, 3)$ in the same energy bins the RPA spectrum consists only of a few

non-collective states and such a scaling procedure can lead to very unrealistic shapes of $\delta\rho_{L\nu}(r)$ with $L = 1$ and 3 which strongly distort the calculated $(\alpha, \alpha')$ cross section for the ISGMR and ISGQR peaks. We have used, therefore, the total RPA transition density as given by the weighted sum (23) of all RPA transition densities in the considered energy bin for the DFM + DWBA calculation of the $(\alpha, \alpha')$ cross section.

To compare our DFM + DWBA results with the inelastic $\alpha$+$^{208}$Pb scattering data at $E_{\rm lab} = 240$ MeV [7], we have generated the total RPA transition densities (23) for the three 640-keV energy bins centered at $E_x = 10.3$, 14.1 and 22.5 MeV, respectively. The total RPA transition density and the two strongest individual RPA transition densities (18) in each energy bin are compared in Fig. 13 with the total collective model transition density (11)-(16) based on $EL$ strengths given by the MDA of the 240 MeV data [7]. While the radial shape of the total RPA transition densities in the energy bins centered at the ISGQR and ISGMR peaks agrees more or less with that of the CM densities, the $EL$ strengths given by the RPA transition densities are much stronger than those given by the CM densities. Such an effect is not unexpected because the predicted $E0$ and $E2$ strengths near the ISGQR and ISQMR peaks are concentrated in just a few discrete RPA states (see upper panels of Figs. 10 and 11). In contrary, the RPA strength for the isoscalar dipole excitation are distributed over many weakly excited $E1$ states, and the total RPA dipole transition density given by the weighted sum (23) of 15 RPA states in the 640-keV bin centered at $E_x = 22.5$ MeV has a slightly weaker $E1$ strength compared to that of the CM transition density. In other words, the RPA calculations of the $E0$ and $E2$ strength do not predict frag-

mentation, at variance with the $E1$ case where the fragmentation caused by Landau damping is quite large. The $EL$ transition strengths given by the total RPA transition densities (23) in the three 640-keV energy bins centered at the ISGMR, ISGQR and ISGDR peaks are given in Table 3.

The DFM + DWBA description of the $(\alpha, \alpha')$ data at 240 MeV [7] given by the RPA transition densities are shown in Fig. 14. Although these DFM + DWBA results agree well with the data, in about the same way as the results given by the CM transition densities, the $EL$ strengths associated with the RPA transition densities in each energy bin are quite different from those given by the CM transition densities (see Table 2). In energy bins centered at the ISGMR and ISGDR peaks the $EL$ transition strengths with $L = 0$ and 2, respectively, are much more dominant compared to those deduced from the MDA of the $(\alpha, \alpha')$ data. For example, only a single RPA transition density (18) of the strongest (discrete) $2^+$ state at the ISGQR peak accounts perfectly for the data measured for the energy bin centered at $E_x = 10.3$ MeV. However, this result should not give the wrong impression that the $EL$ strengths from other multipoles are not as significant as given by the MDA of 240 MeV data [7]. In reality, the isoscalar giant resonances under study are not discrete states as predicted by the RPA but widely fragmented over the excitation energy, having widths $\Gamma \approx 3 \sim 4$ MeV. The physical origin of the observed $EL$ strength fragmentation of the isoscalar giant resonances, in particular their spreading widths, can be described by invoking the anharmonic effects beyond RPA caused by, e.g., the coupling with 2p-2h type configurations (see Refs. [50, 51] for extensive reviews). The inclusion of the anharmonic effects is expected not only to redistribute

the strength of the resonance RPA state over the energy like the averaging procedure (21), but also to pull down the predicted excitation energy to a lower value. We recall again here that the RPA spectrum of $2^+$ states has been shifted down by 2 MeV in energy to have the strongest $2^+$ state near the observed ISGQR peak (see upper panel of Fig. 11); this shift is precisely associated with 2p-2h coupling or in other words, as stated above, to the renormalization of the effective mass $m^*$. Nevertheless, such a perfect agreement of the DWBA cross section predicted by the total RPA transition density with the data measured for the ISGQR peak (see upper panel of Fig. 14) without any fine-tuning of the FF strength is very encouraging. This result confirms the realistic shape of the RPA transition density shown in Fig. 13 and stresses once more the strong predicting power of the RPA approach.

For the ISGMR, the DFM + DWBA calculation using a single transition density (18) for the collective RPA state near the ISGMR peak predicts values of the $(\alpha, \alpha')$ cross section quite close to the data in magnitude but with a deep oscillation pattern that can be smoothed out only by adding the contributions from other multipoles. Such a behavior of the $(\alpha, \alpha')$ cross section calculated for the ISGMR excitation in $^{208}$Pb has been seen in the earlier folding model studies [26, 52]. Although the non-zero multipole $EL$ transition strengths predicted by the RPA for the energy bin centered at $E_x = 14.1$ MeV are somewhat weaker than those given by the MDA of 240 MeV data (see Tables 2 and 3), their contributions are still essential in smoothing out the deep oscillation of the DWBA cross section predicted by the $E0$ transition. Given the quite accurate RPA description of both the

$E0$ strength distribution (upper panel of Fig. 10) and of the $(\alpha, \alpha')$ cross section measured for the ISGMR peak (middle panel of Fig. 14) without any readjustment of the model parameters and shift of the excitation energy, we conclude that the RPA is indeed a reliable theoretical approach to study the GMR excitations in nuclei.

For the ISGDR, the DFM + DWBA calculation using the total RPA transition densities (18) for $L \leq 3$ in the energy bin centered at $E_x = 22.5$ MeV reproduces very well the $(\alpha, \alpha')$ angular distribution measured at 240 MeV (see lower panel of Fig. 14). The main difference between these results and the DFM + DWBA results given by the CM transition densities shown in Fig. 7 is that the RPA predicts quite a strong $E3$ strength in this energy bin ($\sim 10.8\%$) compared to that deduced from the MDA of 240 MeV data ($\sim 5.9\%$), while the $E1$ strength predicted by the RPA is about 60% weaker than the MDA value. As a result, the $E3$ transition turned out to give a dominant contribution to the DWBA cross section for the energy bin centered at $E_x = 22.5$ MeV.

In conclusion, our study of the ISGMR, ISGQR and ISGDR strength distributions and inelastic scattering $(\alpha, \alpha')$ angular distributions measured at the corresponding resonance peaks using the RPA transition densities has shown that the RPA approach can be successfully used to describe not only the $EL$ strength distribution and integral properties of the giant resonances, but also the (double) differential $d^2\sigma/d\Omega dE$ cross sections. Although there are some differences in the $EL$ strengths of non-collective states, the ISGMR, ISGQR and ISGDR strength distributions predicted by the *averaged* RPA results agree reasonably good with those deduced from the MDA of the $(\alpha, \alpha')$

data (see Table 2 and Figs. 10, 11 and 13). The $EL$ transition strengths as well as the location of the ISGQR and ISGDR peaks originally predicted by the RPA are significantly higher than those given by the MDA of the considered $(\alpha, \alpha')$ data. This effect can be qualitatively explained by the lack of the (beyond RPA) anharmonic contributions from, e.g., the 2p-2h coupling.

Therefore, it would be of further interest to perform the same DFM + DWBA analysis including effects beyond the RPA since a self-consistent microscopic calculation beyond RPA coupled to an accurate reaction framework does not exist yet, to our knowledge. The effects, which have been introduced *ad hoc* in the present work via the shift of the RPA mean peak(s) downwards and spreading (21)-(22) of the discrete RPA strength, are exactly those included microscopically into a second RPA, or RPA plus phonon coupling (RPA-PC) calculations (see also Ref. [53]). In this sense, the present results are encouraging. In particular, the effects of 2p-2h coupling on the ISGMR are expected to be small due to well-known cancellation effects and this goes along with the fact that our present simple RPA gives a very good DFM + DWBA description of the monopole excitation.

## 5. Summary

The generalized double-folding approach of Refs. [14, 16] has been further developed for the microscopic study of isoscalar giant resonances induced by inelastic $\alpha$-nucleus scattering, using the nuclear transition densities given by both the collective model and microscopic self-consistent RPA calculation. Although the single-folding approach [15] has been often used to compute

the $\alpha$-nucleus potential in the MDA of the $(\alpha, \alpha')$ data, we have shown in the present work a significant difference in the $(\alpha, \alpha')$ cross sections given by the single- and double-folding methods. The DFM has also been suggested earlier [15, 26] as a more accurate approach to obtain realistic results for the inelastic $\alpha$-nucleus and HI scattering, in particular, the EWSR fractions exhausted by different $EL$ excitation modes. Therefore, the present combination of the DFM and DWBA approaches should be a reliable alternative method to be used in the MDA of future $(\alpha, \alpha')$ measurements.

A reasonable DFM + DWBA description of the 240 MeV $(\alpha, \alpha')$ data in energy bins centered at the ISGMR, ISGQR and ISGDR peaks in $^{208}$Pb has been obtained with the CM nuclear transition densities built upon the $EL$ strengths given by the MDA of these data. Our similar study of the inelastic $\alpha$+$^{208}$Pb scattering at $E_{\rm lab} = 386$ MeV strongly underestimates the data points measured in the same energy bins and, thus, shows quite a strong contribution by the excitation modes of higher multipole ($L > 3$). The contribution by higher multipole excitation modes was found significantly different in the two energy regions around 10 MeV and above 20 MeV, which suggests that the maximum angular momentum $L_{\rm max}$ taken into account in the MDA series (20) should be energy dependent.

The present DFM + DWBA method has also provided an accurate direct link between the *discrete* RPA approach (which was used in the past to describe mainly the integral properties of the giant resonances) and the experimental double differential $(\alpha, \alpha')$ cross sections measured for the resonance peaks. Given high-precision $(\alpha, \alpha')$ data for the isoscalar giant resonances under study, our method can be used in the future to probe the accuracy of

the microscopic prediction by different structure models for the energy distribution of the $S_L(E)$ strength as well as the inelastic scattering $d^2\sigma/d\Omega dE$ cross section. In such a connection, we would like to emphasize again that the latter is very sensitive to the interference of different $EL$ contributions.

## Acknowledgments

We are indebted to Prof. D.H. Youngblood, Prof. T. Kawabata, Dr. X. Chen and Dr. M. Uchida for their helpful communications on the $(\alpha, \alpha')$ data under study. The present research has been supported by National Foundation for Scientific & Technological Development (NAFOSTED) under Project No 103.04.07.09. D.C.C. gratefully acknowledges the financial support from the Asia Link Programme CN/Asia-Link 008 (94791) during his two research stays at the University of Milan where this work has been initiated. Last but not least, one of us (D.T.K.) is grateful to Ray Satchler for his numerous discussions during the years of collaboration, which have laid the foundation for this research study.

## References

[1] M.N. Harakeh, A. van der Woude, *Giant Resonances: Fundamental High-Frequency Modes of Nuclear Excitation*, Clarendon Press, Oxford, 2001; P.F. Bortignon, A. Bracco, R.A. Broglia, *Giant Resonances; Nuclear Structure at Finite Temperature*, Harwood Academic, New York, 1998.

[2] S. Shlomo, V.M. Kolomietz, G. Colò, Eur. Phys. J. A 30 (2006) 23-30.

[3] G. Colò, Physics of Particles and Nuclei 39 (2008) 286-326.

[4] M.N. Harakeh, K. van der Borg, T. Ishimatsu, H.P. Morsch, A. van der Woude, and F.E. Bertrand, Phys. Rev. Lett. 38 (1977) 676-679.

[5] M.N. Harakeh, B. van Heyst, K. van der Borg, A. van der Woude, Nucl. Phys. A 327 (1979) 373-396.

[6] D.H. Youngblood, C.M. Rozsa, J.M. Moss, D.R. Brown, J.D. Bronson, Phys. Rev. Lett. 39 (1977) 1188-1191.

[7] D.H. Youngblood, Y.W. Lui, H.L. Clark, B. John, Y. Tokimoto, X. Chen, Phys. Rev. C 69 (2004) 034315; D.H. Youngblood, X. Chen, private communication (unpublished).

[8] M. Uchida, H. Sakaguchi, M. Itoh, M. Yosoi, T. Kawabata, H. Takeda, Y. Yasuda, T. Murakami, T. Ishikawa, T. Taki, N. Tsukahara, S. Terashima, U. Garg, M. Hedden, B. Kharraja, M. Koss, B. K. Nayak, S. Zhu, M. Fujiwara, H. Fujimura, K. Hara, E. Obayashi, H.P. Yoshida, H. Akimune, M.N. Harakeh, M. Volkerts, Phys. Lett. B 557 (2003) 12-19.

[9] M. Uchida, H. Sakaguchi, M. Itoh, M. Yosoi, T. Kawabata, Y. Yasuda, H. Takeda, T. Murakami, S. Terashima, S. Kishi, U. Garg, P. Boutachkov, M. Hedden, B. Kharraja, M. Koss, B.K. Nayak, S. Zhu, M. Fujiwara, H. Fujimura, H.P. Yoshida, K. Hara, H. Akimune, M.N. Harakeh, Phys. Rev. C 69 (2004) 051301(R); T. Kawabata, M. Uchida, private communication (unpublished).

[10] M.N. Harakeh, A.E.L. Dieperink, Phys. Rev. C 23 (1981) 2329-2334.

[11] N.V. Giai, H. Sagawa, Nucl. Phys. A 371 (1981) 1-18.

[12] B.F. Davis, U. Garg, W. Reviol, M.N. Harakeh, A. Bacher, G.P. A. Berg, C.C. Foster, E.J. Stephenson, Y. Wang, J. Jänecke, K. Pham, D. Roberts, H. Akimune, M. Fujiwara, J. Lisantti, Phys. Rev. Lett. 79 (1997) 609-612.

[13] G.R. Satchler, *Direct Nuclear Reactions*, Clarendon Press, Oxford, 1983.

[14] D.T. Khoa, G.R. Satchler, Nucl. Phys. A 668 (2000) 3-41.

[15] G.R. Satchler, D.T. Khoa, Phys. Rev. C 55 (1997) 285-297.

[16] D.T. Khoa, G.R. Satchler, W. von Oertzen, Phys. Rev. C 56 (1997) 954-969.

[17] D.T. Khoa, W. von Oertzen, H.G. Bohlen, S. Ohkubo, J. Phys. G 34 (2007) R111-R164.

[18] J.P. Jeukenne, A. Lejeune, C. Mahaux, Phys. Rev. C 16 (1977) 80-96.

[19] D.T. Khoa, D.C. Cuong, Phys. Lett. B 660 (2008) 331-338.

[20] N. Anantaraman, H. Toki, G.F. Bertsch, Nucl. Phys. A 398 (1983) 269-278.

[21] A. Ingemarsson, J. Nyberg, P.U. Renberg, O. Sundberg, R.F. Carlson, A.J. Cox, A. Auce, R. Johansson, G. Tibell, D.T. Khoa, R. E. Warner, Nucl. Phys. A 676 (2000) 3-31.

[22] B. Bonin, N. Alamanos, B. Berthier, G. Bruge, H. Faraggi, J.C. Lugol, W. Mittig, L. Papineau, A.I. Yavin, J. Arvieux, L. Farvacque, M. Buenerd, W. Bauhoff, Nucl. Phys. A 445 (1985) 381-407.

[23] D.T. Khoa, Phys. Rev. C 63 (2001) 034007.

[24] W.G. Love, Nucl. Phys. A 312 (1978) 160-176.

[25] F. Carstoiu, M. Lassaut, Nucl. Phys. A 597 (1996) 269-297.

[26] D.J. Horen, J.R. Beene, G.R. Satchler, Phys. Rev. C 52 (1995) 1554-1564.

[27] A. Bohr, B.R. Mottelson, *Nuclear Structure*, W.A. Benjamin, Reading, 1975, vol. II.

[28] M.E. Farid, G.R. Satchler, Nucl. Phys. A 438 (1985) 525-535.

[29] H. Überall, *Electron Scattering from Complex Nuclei*, Academic Press, New York, 1971, vol. B.

[30] A. van der Woude, Nucl. Phys. A 649 (1999) 97c-103c.

[31] D.T. Khoa, E. Khan, G. Colò, N.V. Giai, Nucl. Phys. A 706 (2002) 61-84.

[32] J. Guillot, S. Galès, D. Beaumel, S. Fortier, E. Rich, N. Van Giai, G. Colò, A.M. van der Berg, S. Brandenburg, B. Davids, M.N. Harakeh, M. Hunyadi, M. de Huu, S.Y. van der Werf, H.J. Wörtche, C. Bäumer, D. Frekers, E.W. Grewe, P. Haefner, B.C. Junk, M. Fujiwara, Phys. Rev. C 73 (2006) 014616.

[33] E. Chabanat, P. Bonche, P. Haensel, J. Meyer, R. Schaeffer, Nucl. Phys. A 635 (1998) 231-256.

[34] G. Colò, P.F. Bortignon, S. Fracasso, N. V. Giai, Nucl. Phys. A 788 (2007) 137c-181c.

[35] G.R. Satchler, W.G. Love, Phys. Rep. 55 (1979) 183-254.

[36] T. Kibedi, R.H. Spear, At. Data and Nucl. Data Tables 80 (2002) 35-82.

[37] G. Colò, N. Van Giai, J. Meyer, K. Bennaceur, P. Bonche, Phys. Rev. C 70 (2004) 024307.

[38] D. Vretenar, T. Nikšić, P. Ring, Phys. Rev. C 68 (2003) 024310.

[39] M. Uchida, PhD Thesis (University of Kyoto, 2003).

[40] S. Stringari, Phys. Lett. 108 B (1982) 232-236.

[41] J.P. Blaizot, J.F. Berger, J. Dechargé, M. Girod, Nucl. Phys. A 591 (1995) 435-457.

[42] D.T. Khoa, I.N. Kuchtina, V.Yu. Ponomarev, Sov. J. Nucl. Phys. 44 (1986) 585-590.

[43] D.J. Horen, G.R. Satchler, S.A. Fayans, E.L. Trykov, Nucl. Phys. A 600 (1996) 193-235.

[44] A. Kolomiets, O. Pochivalov, S. Shlomo, Phys. Rev. C 61 (2000) 034312.

[45] H. Feshbach, *Theoretical Nuclear Physics - Nuclear Reactions*, Wiley, New York, 1992.

[46] G. Colò, N.V. Giai, P.F. Bortignon, M.R. Quaglia, Phys. Lett. B 485 (2000) 362-366.

[47] D. Vretenar, A. Wandelt, P. Ring, Phys. Lett. B 487 (2000) 334-340.

[48] J. Piekarewicz, Phys. Rev. C 64 (2001) 024307.

[49] S.I. Bastrukov, S. Misicu, V.I. Sushkov, Nucl. Phys. A 562 (1993) 191; S. Misicu, Phys. Rev. C 73 (2006) 024301; D. Vretenar, N. Paar, P. Ring, T. Nikšić, Phys. Rev. C 65 (2002) 021301(R).

[50] G.F. Bertsch, P.F. Bortignon, R.A. Broglia, Rev. Mod. Phys. 55 (1983) 287-314.

[51] S. Drozdz, S. Nishizaki, J. Speth, J. Wambach, Phys. Rep. 197 (1990) 1-65.

[52] F.E. Bertrand, G.R. Satchler, D.J. Horen, J.R. Wu, A.D. Bacher, G.T. Emery, W.P. Jones, D.W. Miller, A. van der Woude, Phys. Rev. C 22 (1980) 1832-1847.

[53] V. Tselyaev, J. Speth, S. Krewald, E. Litvinova, S. Kamerdzhiev, N. Lyutorovich, A. Adveenkov, F. Grümmer, Phys. Rev. C79 (2009) 034309.

## Figure captions

Fig.1: Upper panel: OM description of the elastic $\alpha$+$^{208}$Pb scattering data at 240 MeV [7] and 386 MeV [8, 9] given by the unrenormalized (dash curves) and renormalized complex folded OP (solid curves). Lower panel: DWBA descriptions of the inelastic $\alpha$+$^{208}$Pb scattering data [7, 8, 9] for $3^-_1$ state of $^{208}$Pb ($E_x = 2.61$ MeV) given by the collective model (dash curves) and RPA (solid curves) nuclear transition densities.

Fig.2: Inelastic $\alpha$+$^{208}$Pb scattering data at $E_{\rm lab} = 240$ MeV measured for the energy bin centered at $E_x = 14.1$ MeV [7] in comparison with the DFM + DWBA results given by the CM transition densities based on the isoscalar $EL$ strengths taken from Refs. [7] (lower panel) and [8] (upper panel). See details in the text and Table 2.

Fig.3: Inelastic $\alpha$+$^{208}$Pb scattering data at $E_{\rm lab} = 386$ MeV measured for the energy bin centered at $E_x = 13.5$ MeV [39] in comparison with the DFM + DWBA results given by the CM transition densities based on the isoscalar $EL$ strengths taken from Refs. [7] (lower panel) and [8, 9] (upper panel). See details in the text and Table 2.

Fig.4: Inelastic $\alpha$+$^{208}$Pb scattering data at $E_{\rm lab} = 386$ MeV measured for the energy bin centered at $E_x = 14.5$ MeV [39] in comparison with the DWBA results given by the isoscalar $EL$ strengths taken from Refs. [8, 9]. Upper panel: the present DFM + DWBA calculation; lower panel: the MDA results by Uchida *et al.* [8, 9].

Fig.5: The same as Fig. 2 but for the energy bin centered at $E_x = 10.3$ MeV.

Fig.6: The same as Fig. 3 but for the energy bin centered at $E_x = 10.5$ MeV.

Fig.7: The same as Fig. 2 but for the energy bin centered at $E_x = 22.5$ MeV.

Fig.8: The same as Fig. 3 but for the energy bin centered at $E_x = 22.5$ MeV.

Fig.9: Inelastic $\alpha$+$^{208}$Pb scattering data at $E_{\rm lab} = 386$ MeV measured for the energy bins centered at $E_x = 10.5$ and 22.5 MeV [39] in comparison with the DWBA results given by the isoscalar $EL$ strengths taken from Refs. [8, 9]. Solid curves: the present DFM + DWBA calculation; dashed curves: the MDA results by Uchida *et al.* [8, 9]; dashed-dotted curves: the same as dashed curves but using microscopic Coulomb FF from the present DFM calculation.

Fig.10: Isoscalar $E0$ strength distributions deduced from the MDA analyses of inelastic $\alpha$+$^{208}$Pb scattering data at 240 MeV by Youngblood *et al.* [7] and 386 MeV by Uchida *et al.* [8, 39] in comparison with the RPA results. See details in text.

Fig.11: The same as Fig. 10 but for the isoscalar $E2$ strength distributions.

Fig.12: The same as Fig. 10 but for the isoscalar $E1$ strength distributions.

Fig.13: Total RPA transition density (23) and transition densities of the two strongest RPA states in the 640-keV energy bins centered at $E_x = 10.3$, 14.1 and 22.5 MeV, respectively. The corresponding collective model transition densities were built upon the $EL$ strengths given by the MDA of 240

MeV data [7]. The quoted percentages are the exhausted fractions of the isoscalar $EL$ EWSR.

Fig.14: Inelastic $\alpha$+$^{208}$Pb scattering data at $E_{\rm lab}$ = 240 MeV measured for the 640 keV energy bins centered at $E_x$ = 10.3, 14.1 and 22.5 MeV respectively [7], in comparison with the DFM + DWBA results obtained with the total RPA transition densities (23) which give the fractions of the isoscalar $EL$ EWSR shown in Table 3.

Table 1: Parameters of the complex density dependence of the CDM3Y6 interaction (3)-(4) used to calculate the OP and inelastic scattering FF for the elastic and inelastic $\alpha$+$^{208}$Pb scattering at $E_{\rm lab}$ = 240 and 386 MeV. $N_{\rm R(I)}$ are the renormalization coefficients of the real and imaginary OP given by the optical model analysis of elastic scattering data; $\sigma_{\rm R}$ is the calculated total reaction cross section.

| $E_{\rm lab}$ (MeV) | $x$ | $C_x$ | $\alpha_x$ | $\beta_x$ (fm$^3$) | $\gamma_x$ (fm$^3$) | $N_x$ | $\sigma_{\rm R}$ (mb) | $\sigma_{\rm R}^{\rm exp}$ (mb) |
|---|---|---|---|---|---|---|---|---|
| 240 | R | 0.2243 | 3.8033 | 1.4099 | -4.0 | 0.9043 | 2768 | 2900±190 [a] |
| | I | 0.1897 | 2.4840 | 5.1831 | -3.1341 | 1.4052 | | |
| 386 | R | 0.1991 | 3.8033 | 1.4099 | -4.0 | 0.9885 | 2754 | 2884±87 [b] |
| | I | 0.1435 | 3.1541 | 2.5646 | -2.5089 | 1.3565 | | |

[a] Experimental total reaction cross section measured at $E_{\rm lab}$ = 192 MeV [21]

[b] Experimental total reaction cross section measured at $E_{\rm lab}$ = 340 MeV [22]

Table 2: Fractions of the isoscalar $EL$ EWSR exhausted in energy bin centered at the excitation energy $E_x$ deduced from the MDA analyses of inelastic $\alpha$+$^{208}$Pb scattering data at $E_{\rm lab}$ = 240 [7] and 386 MeV [8, 9], and from the *averaged* RPA results. The averaging of RPA transition densities (<RPA>) is discussed below in Sec. 4. $\delta_L$ are the deformation lengths for the CM nuclear transition densities (11)-(16) based on the $EL$ strengths taken from Ref. [7].

| $E_x$ (MeV) | | $L^\pi$ | $100 \times a_L(E_x)$ (% EWSR/MeV) | | | $\delta_L$ (fm) |
|---|---|---|---|---|---|---|
| [7] | [8, 9] | | MDA [7] | MDA [8, 9] | <RPA> | MDA [7] |
| 10.3 | 9.5 | $0^+$ | $1.88 \pm 0.70$ | $2.68 \pm 0.47$ | 2.74 | 0.0086 |
| | | $1^-$ | $2.63 \pm 0.65$ | $2.20 \pm 0.23$ | 1.39 | 0.0012 |
| | | $2^+$ | $20.5 \pm 1.11$ | $12.4 \pm 0.40$ | 13.3 | 0.2928 |
| | | $3^-$ | 0.0 | $3.48 \pm 0.18$ | 1.06 | 0.0 |
| 10.9 | 10.5 | $0^+$ | $3.13 \pm 0.70$ | $3.74 \pm 0.65$ | 2.74 | 0.0111 |
| | | $1^-$ | $3.01 \pm 0.50$ | $3.12 \pm 0.45$ | 1.27 | 0.0014 |
| | | $2^+$ | $23.4 \pm 1.51$ | $19.0 \pm 0.80$ | 13.7 | 0.3094 |
| | | $3^-$ | $12.3 \pm 0.20$ | $4.27 \pm 0.46$ | 1.07 | 0.3354 |
| 14.1 | 13.5 | $0^+$ | $37.6 \pm 0.62$ | $16.0 \pm 1.86$ | 16.6 | 0.0329 |
| | | $1^-$ | $6.26 \pm 0.42$ | $6.03 \pm 0.78$ | 1.68 | 0.0018 |
| | | $2^+$ | $6.59 \pm 1.79$ | $14.9 \pm 0.80$ | 3.12 | 0.1416 |
| | | $3^-$ | 0.0 | $3.40 \pm 0.76$ | 1.43 | 0.0 |
| 14.8 | 14.5 | $0^+$ | $20.8 \pm 0.90$ | $12.4 \pm 1.60$ | 16.2 | 0.0243 |
| | | $1^-$ | $5.45 \pm 0.32$ | $4.90 \pm 0.52$ | 1.85 | 0.0016 |
| | | $2^+$ | $4.75 \pm 2.26$ | $13.2 \pm 1.40$ | 2.73 | 0.1185 |
| | | $3^-$ | 0.0 | $4.49 \pm 0.68$ | 1.48 | 0.0 |
| 22.5 | 22.5 | $0^+$ | 0.0 | $2.22 \pm 1.26$ | 1.29 | 0.0 |
| | | $1^-$ | $8.23 \pm 0.15$ | $8.67 \pm 0.59$ | 7.06 | 0.0016 |
| | | $2^+$ | 0.0 | $10.4 \pm 1.70$ | 0.60 | 0.0 |
| | | $3^-$ | $5.90 \pm 0.30$ | $5.42 \pm 0.95$ | 4.74 | 0.1584 |

Table 3: Fractions of the isoscalar $EL$ EWSR exhausted in the 640-keV energy bin centered at the excitation energy $E_x$ determined from the RPA transition strengths.

| % EWSR/MeV | | | |
|---|---|---|---|
| $L^\pi$ | $E_x = 10.3$ MeV | $E_x = 14.1$ MeV | $E_x = 22.5$ MeV |
| $0^+$ | 1.25 | 55.1 | 0.06 |
| $1^-$ | 0.32 | 2.25 | 5.45 |
| $2^+$ | 61.7 | 0.34 | 0.06 |
| $3^-$ | 0.69 | 0.83 | 10.8 |

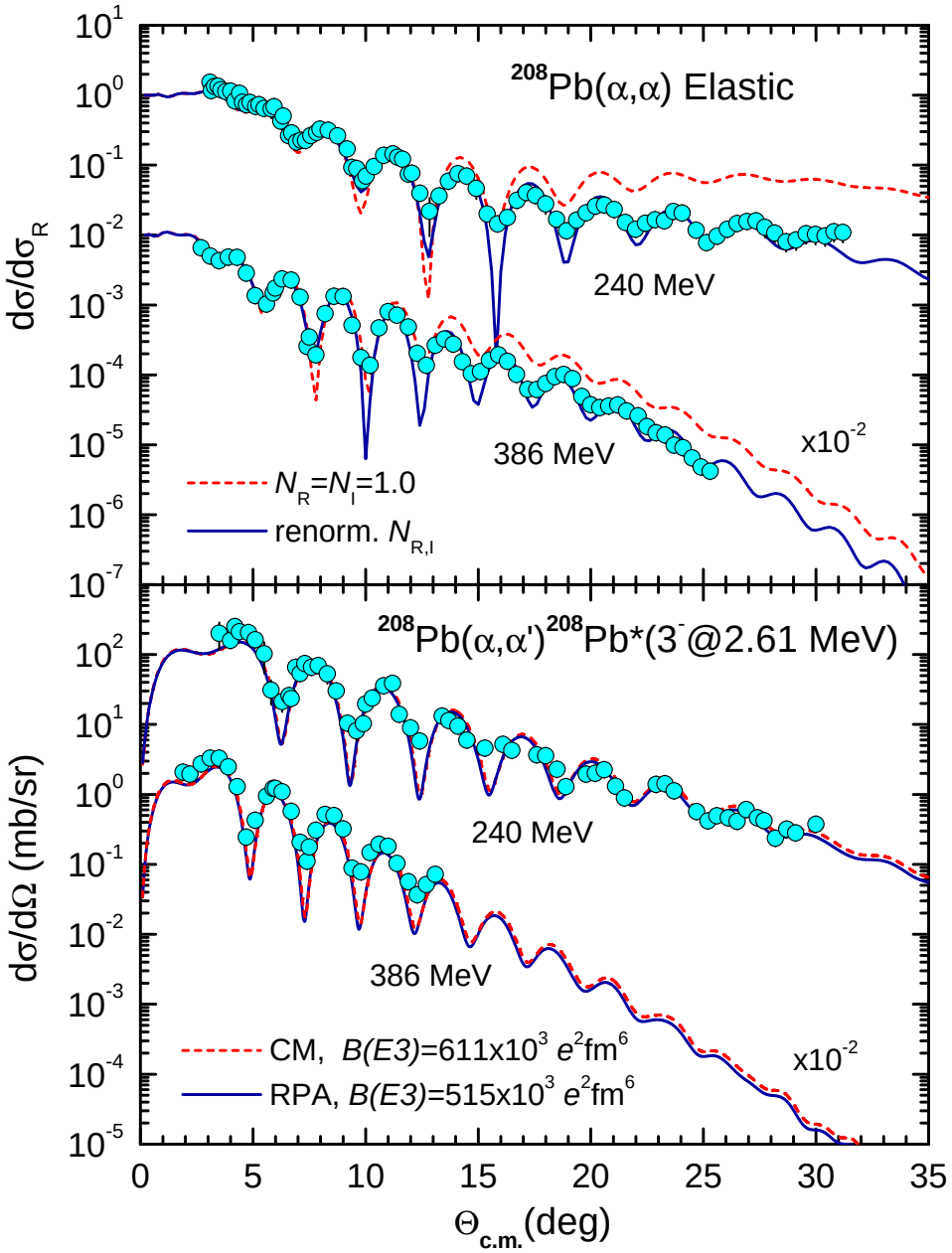


Figure 1: Upper panel: OM description of the elastic $\alpha$+$^{208}$Pb scattering data at 240 MeV [7] and 386 MeV [8, 9] given by the unrenormalized (dash curves) and renormalized complex folded OP (solid curves). Lower panel: DWBA descriptions of the inelastic $\alpha$+$^{208}$Pb scattering data [7, 8, 9] for $3_1^-$ state of $^{208}$Pb ($E_x$ = 2.61 MeV) given by the collective model (dash curves) and RPA (solid curves) nuclear transition densities.

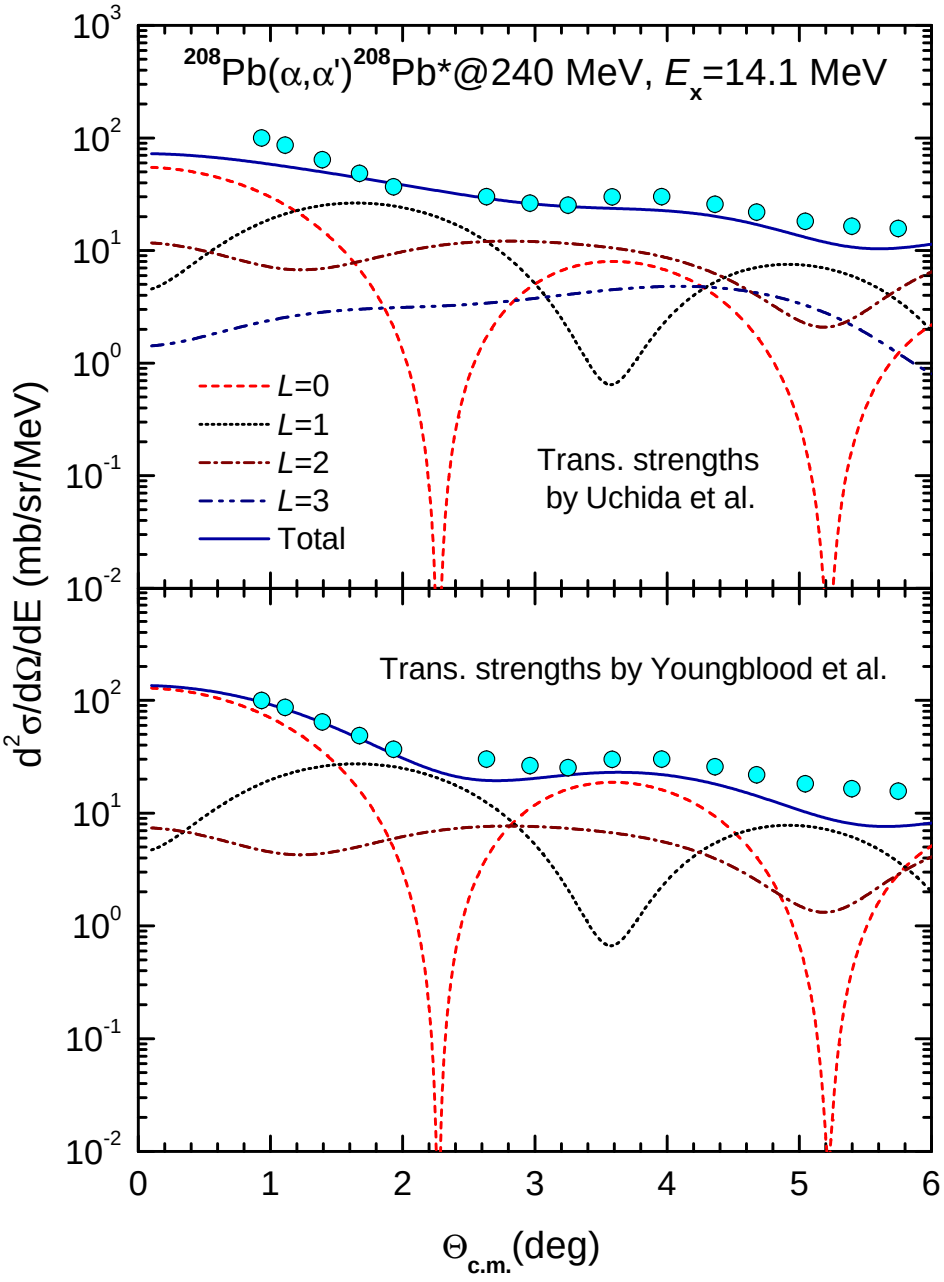


Figure 2: Inelastic $\alpha$+$^{208}$Pb scattering data at $E_{\rm lab}$ = 240 MeV measured for the energy bin centered at $E_x$ = 14.1 MeV [7] in comparison with the DFM + DWBA results given by the CM transition densities based on the isoscalar $EL$ strengths taken from Refs. [7] (lower panel) and [8] (upper panel). See details in the text and Table 2.

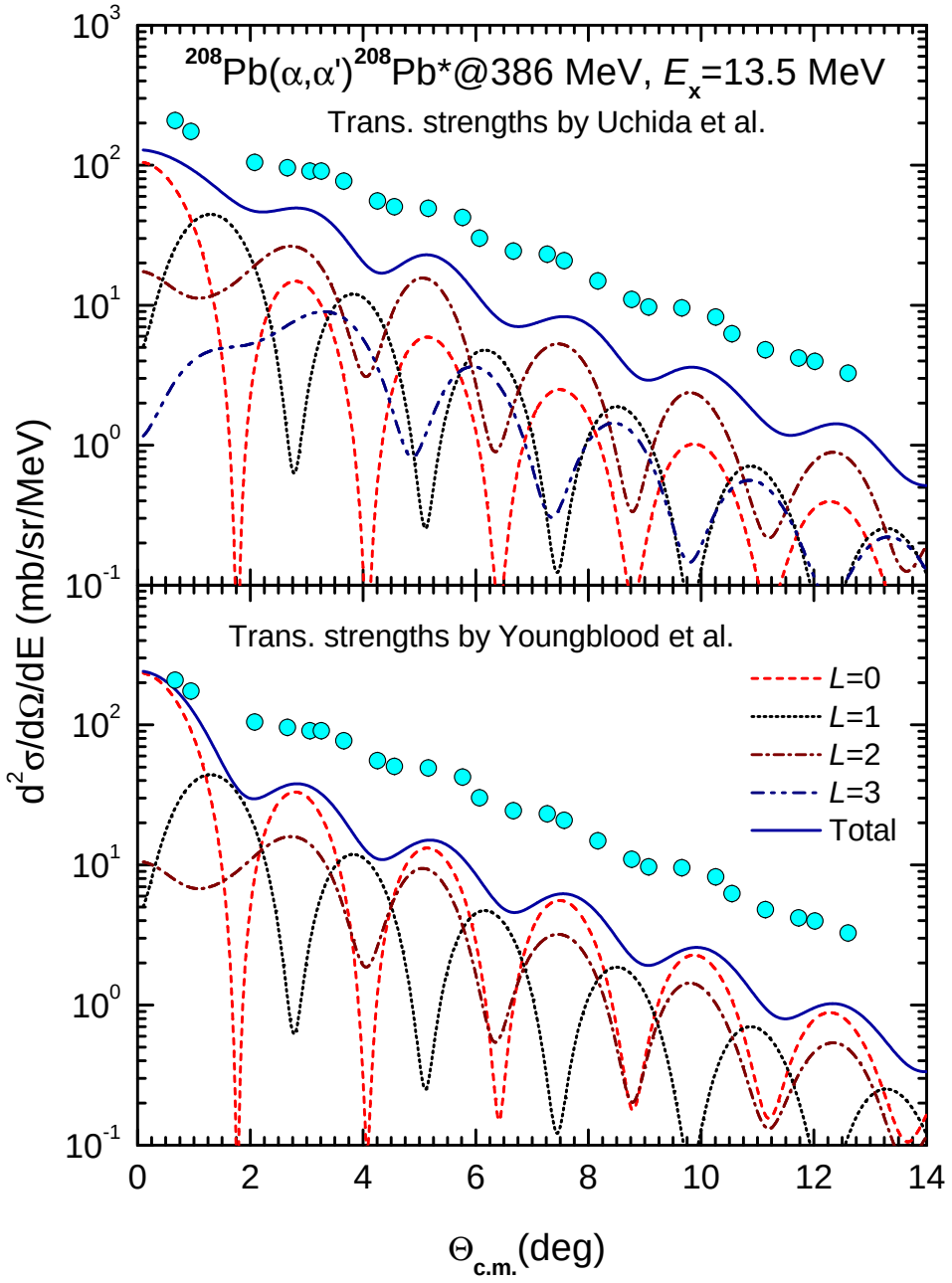


Figure 3: Inelastic $\alpha$+$^{208}$Pb scattering data at $E_{\rm lab}$ = 386 MeV measured for the energy bin centered at $E_x$ = 13.5 MeV [39] in comparison with the DFM + DWBA results given by the CM transition densities based on the isoscalar $EL$ strengths taken from Refs. [7] (lower panel) and [8, 9] (upper panel). See details in the text and Table 2.

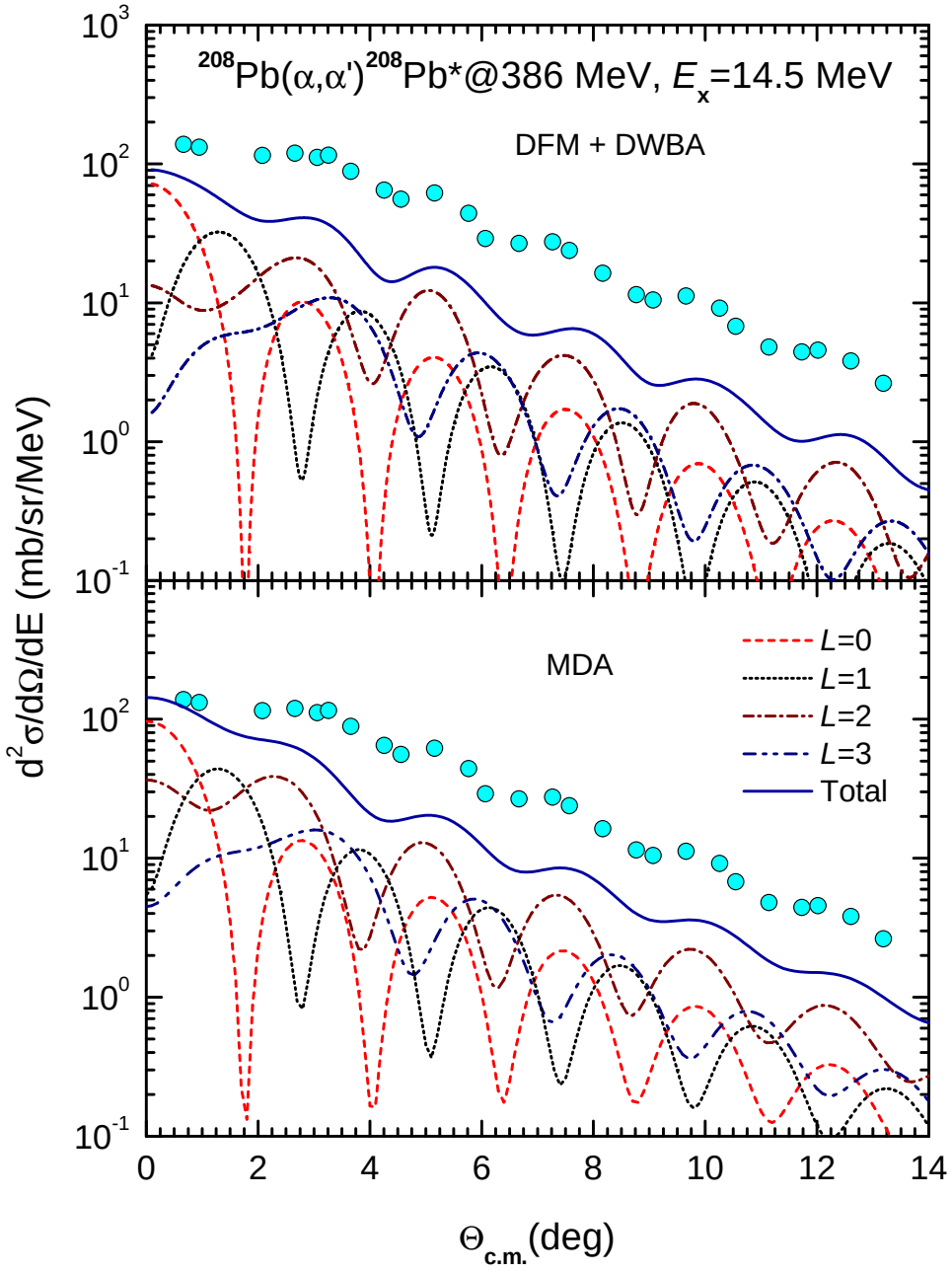


Figure 4: Inelastic $\alpha$+$^{208}$Pb scattering data at $E_{\rm lab}$ = 386 MeV measured for the energy bin centered at $E_x$ = 14.5 MeV [39] in comparison with the DWBA results given by the isoscalar $EL$ strengths taken from Refs. [8, 9]. Upper panel: the present DFM + DWBA calculation; lower panel: the MDA results by Uchida *et al.* [8, 9].

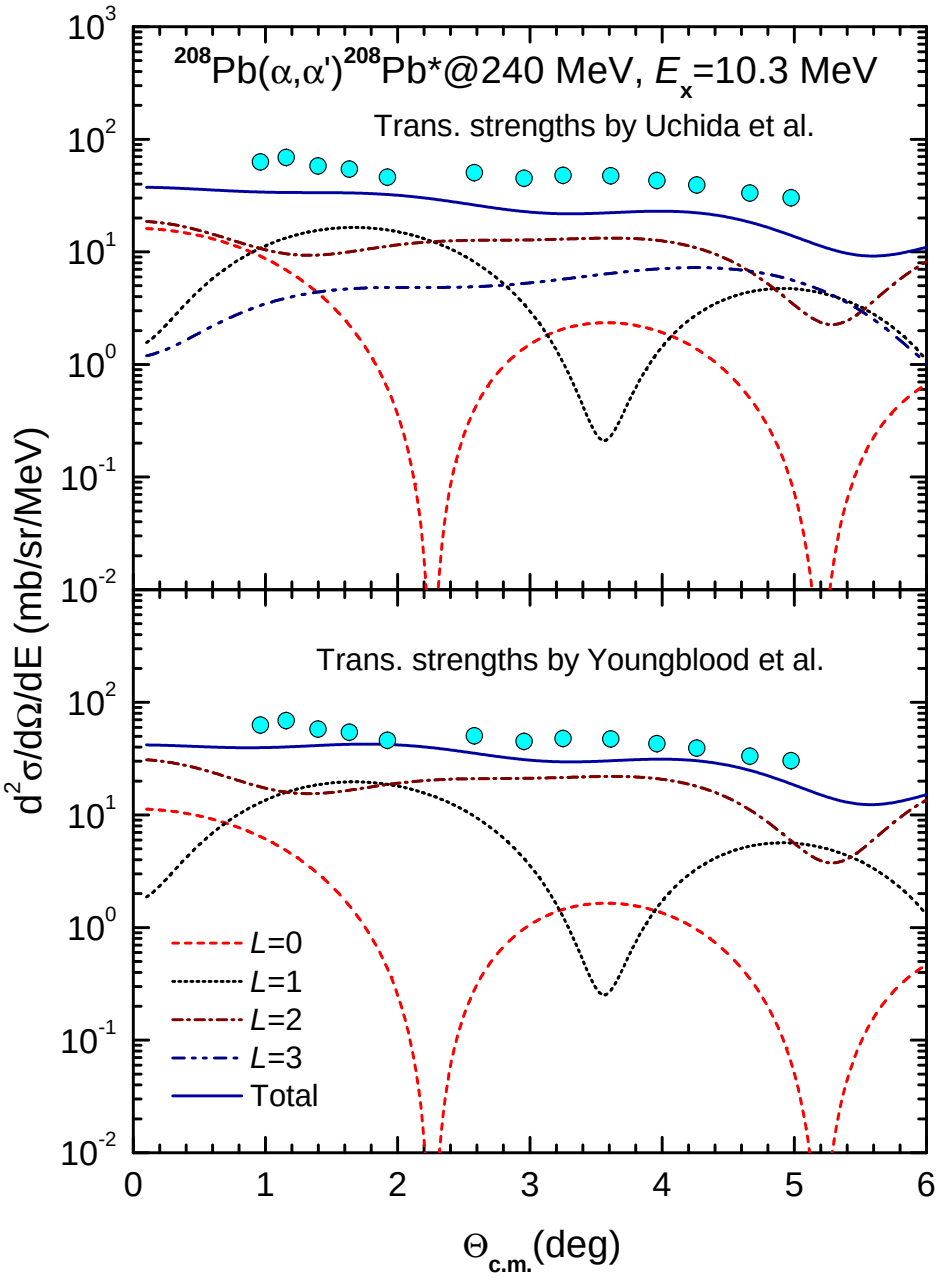


Figure 5: The same as Fig. 2 but for the energy bin centered at $E_x = 10.3$ MeV.

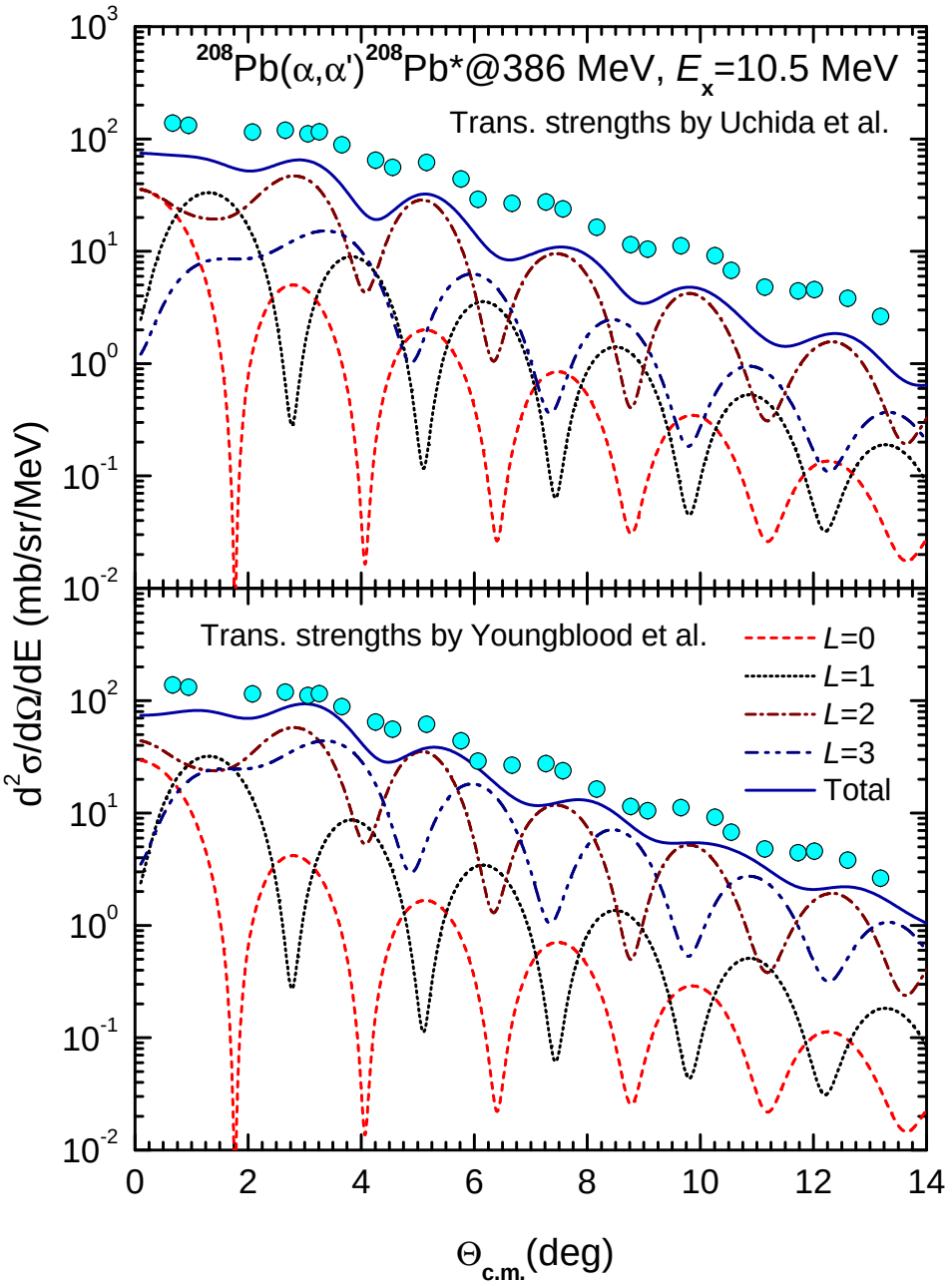


Figure 6: The same as Fig. 3 but for the energy bin centered at $E_x = 10.5$ MeV.

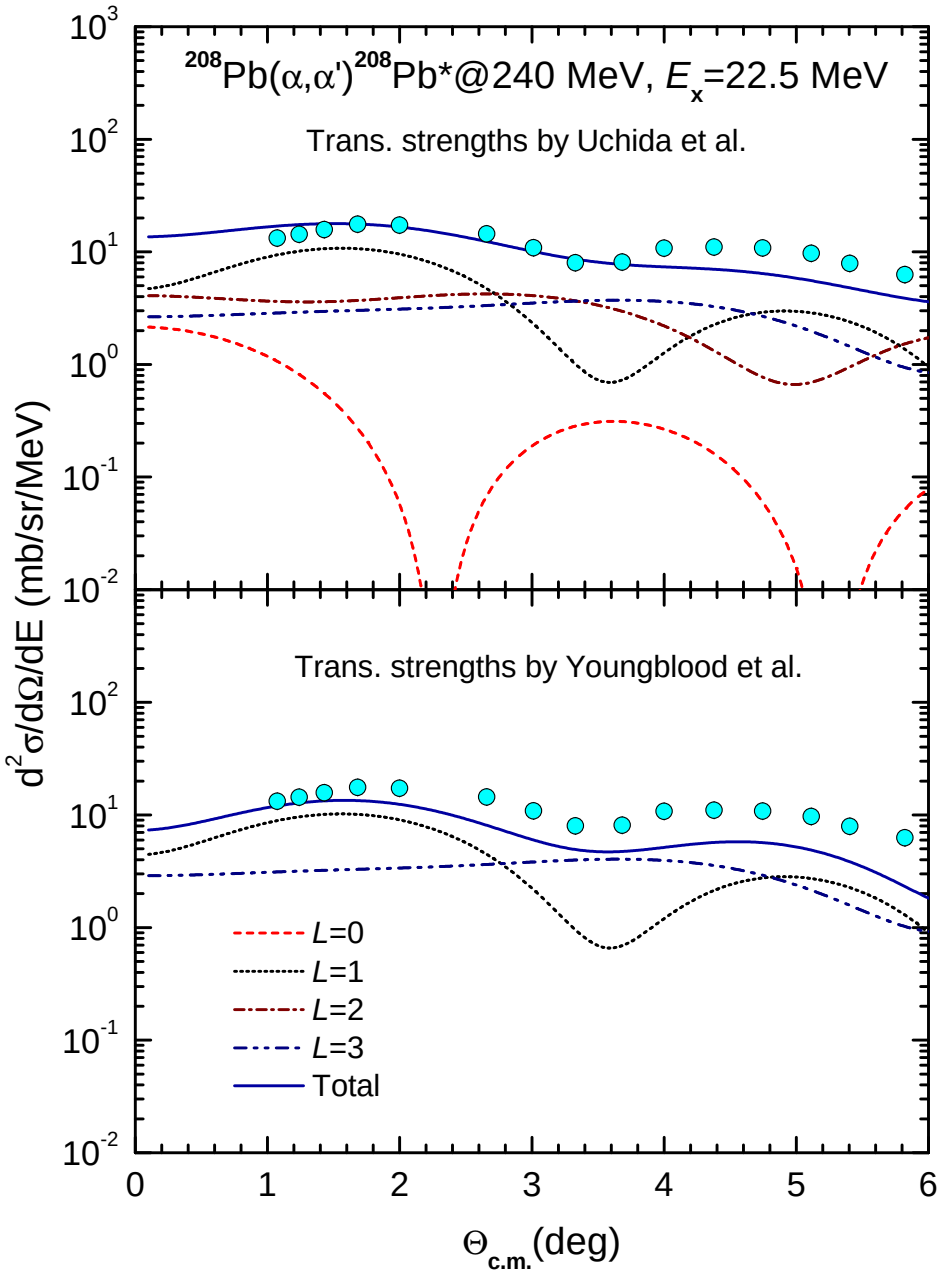


Figure 7: The same as Fig. 2 but for the energy bin centered at $E_x = 22.5$ MeV.

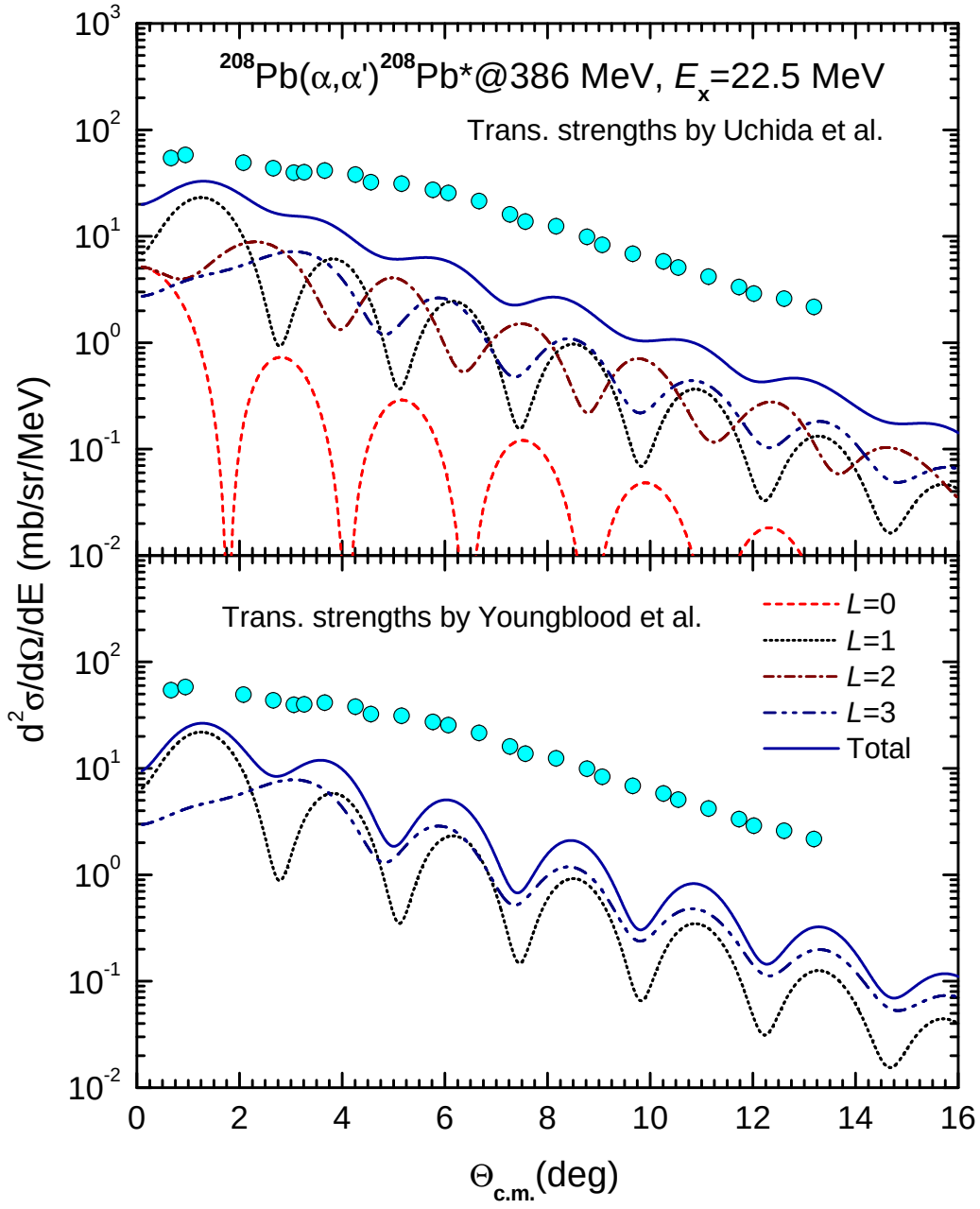


Figure 8: The same as Fig. 3 but for the energy bin centered at $E_x = 22.5$ MeV.

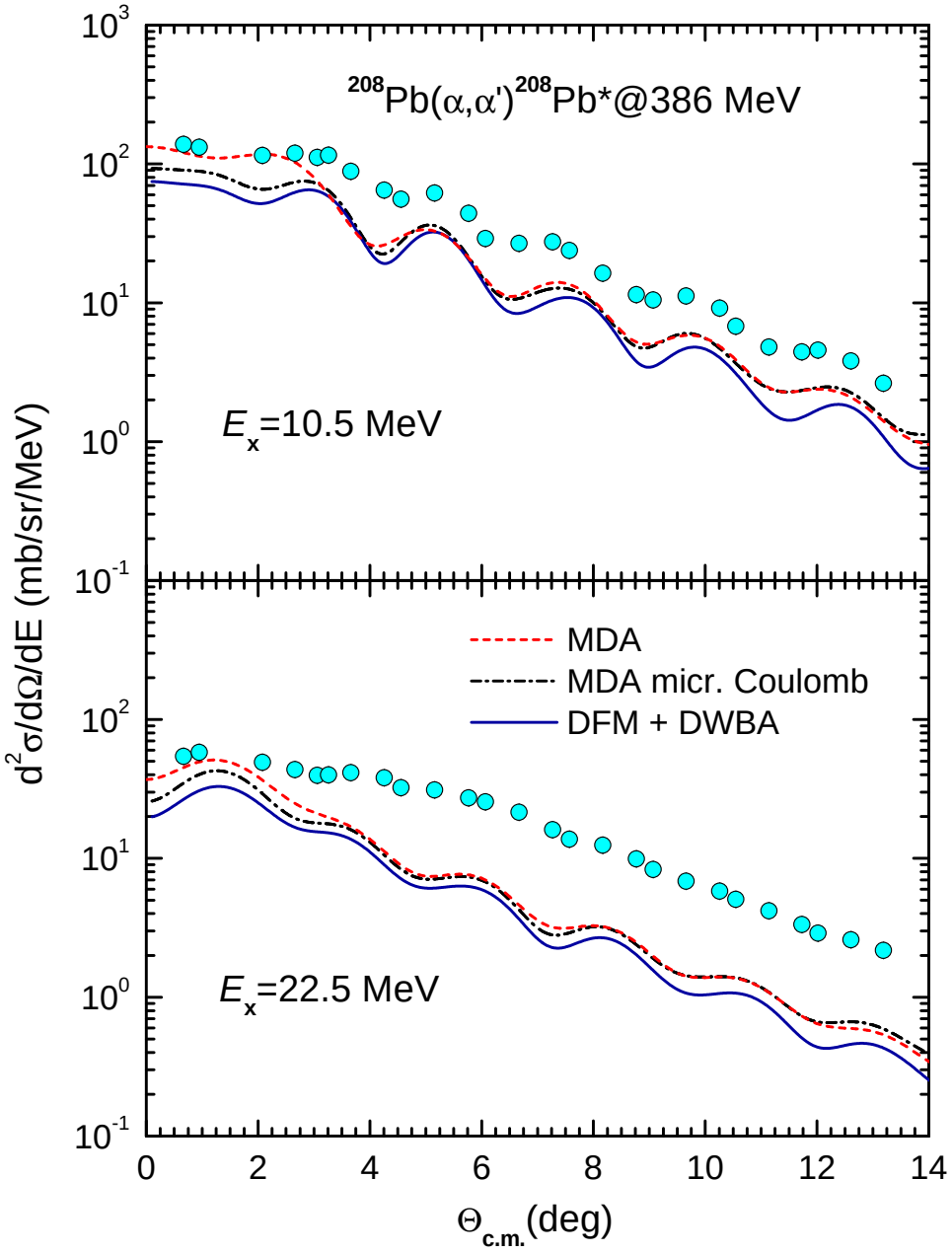


Figure 9: Inelastic $\alpha$+$^{208}$Pb scattering data at $E_{\rm lab}$ = 386 MeV measured for the energy bins centered at $E_x$ = 10.5 and 22.5 MeV [39] in comparison with the DWBA results given by the isoscalar $EL$ strengths taken from Refs. [8, 9]. Solid curves: the present DFM + DWBA calculation; dashed curves: the MDA results by Uchida *et al.* [8, 9]; dashed-dotted curves: the same as dashed curves but using microscopic Coulomb FF from the present DFM calculation.

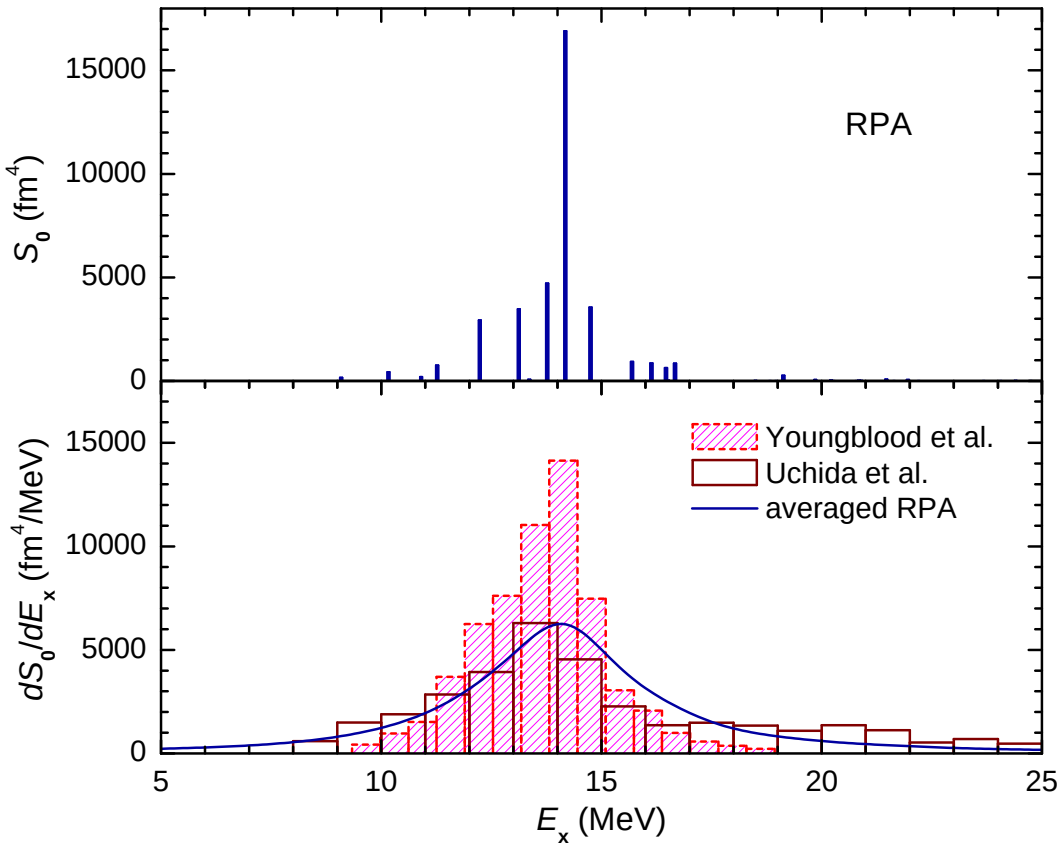


Figure 10: Isoscalar $E0$ strength distributions deduced from the MDA analyses of inelastic $\alpha$+$^{208}$Pb scattering data at 240 MeV by Youngblood *et al.* [7] and 386 MeV by Uchida *et al.* [8, 39] in comparison with the RPA results. See details in text.

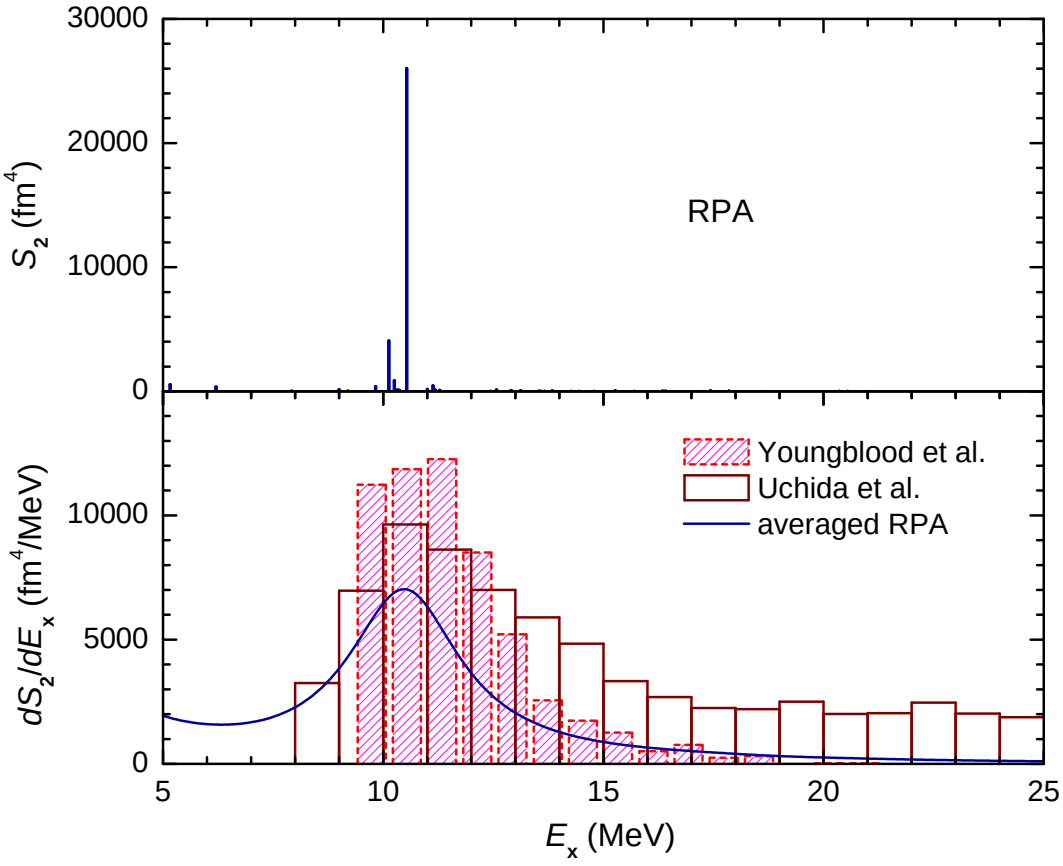


Figure 11: The same as Fig. 10 but for the isoscalar $E2$ strength distributions.

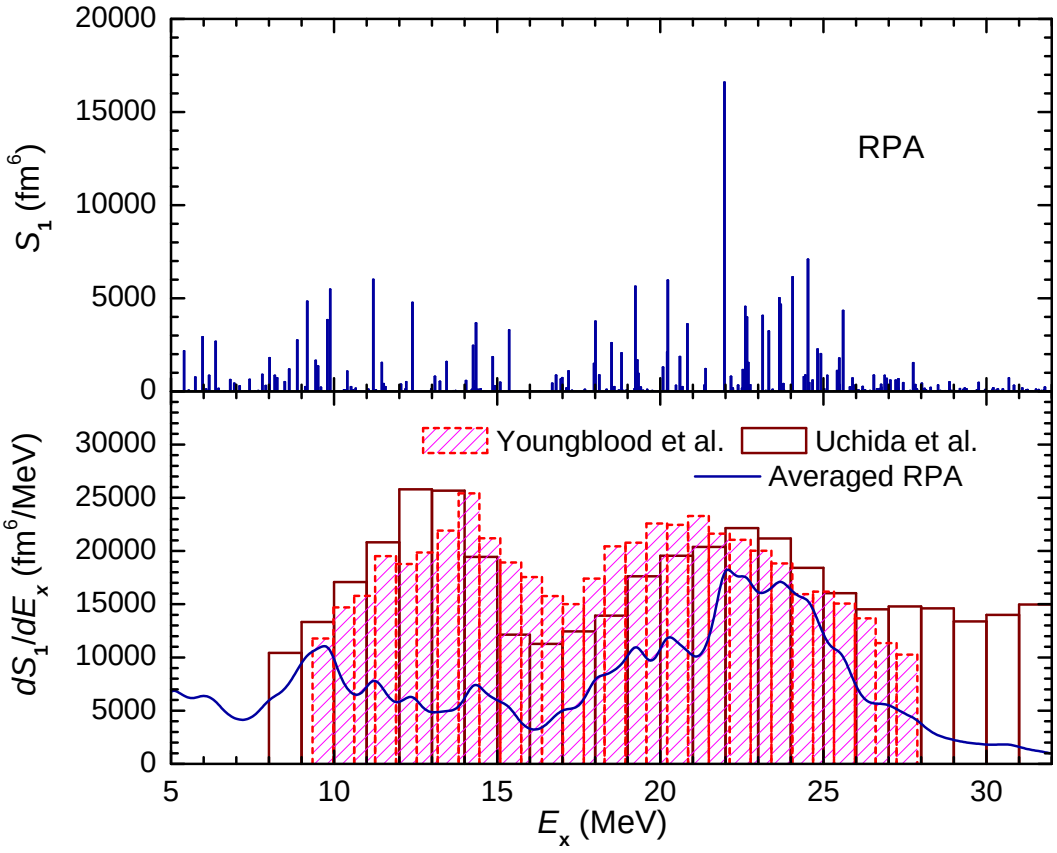


Figure 12: The same as Fig. 10 but for the isoscalar $E1$ strength distributions.

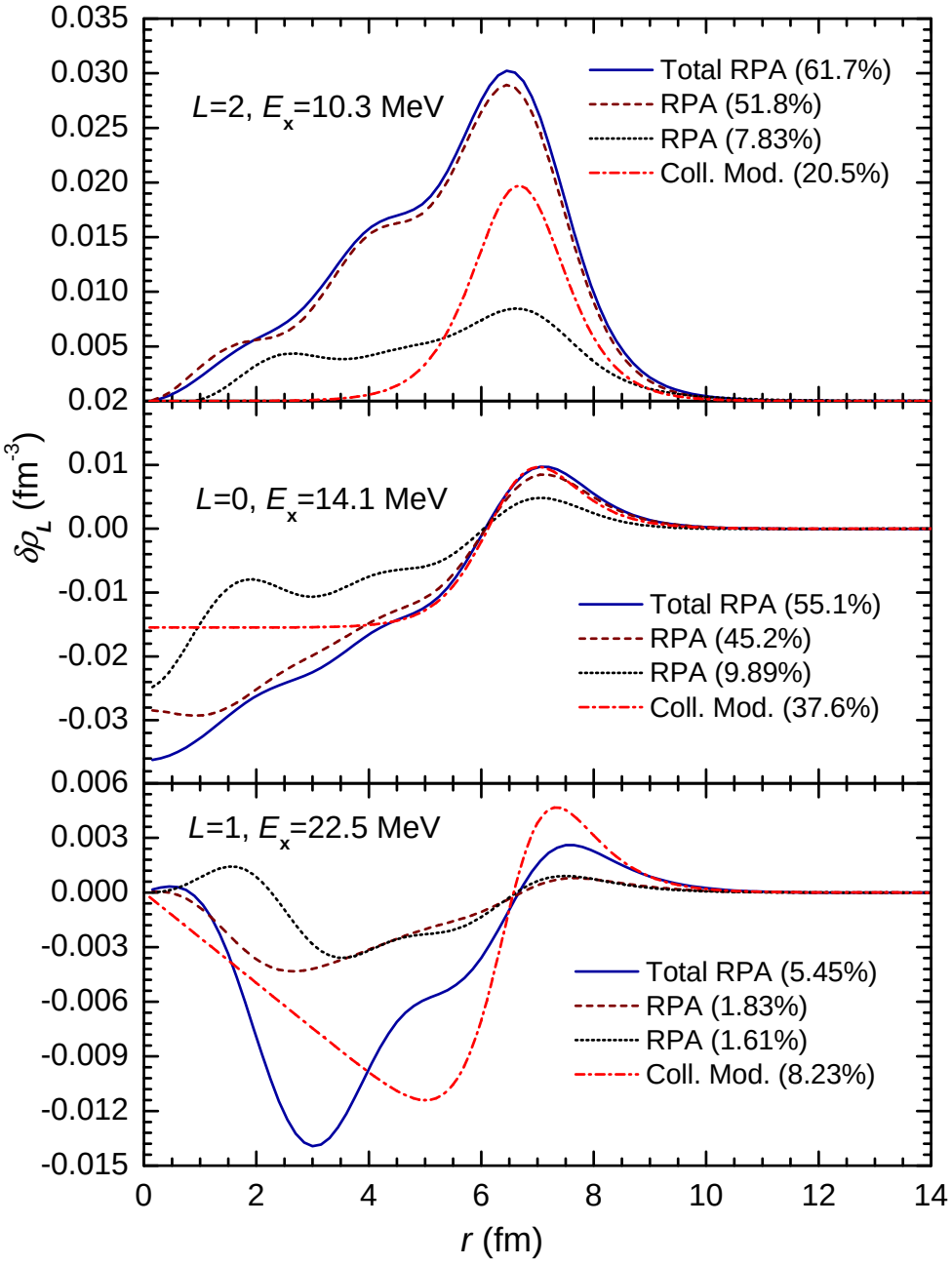


Figure 13: Total RPA transition density (23) and transition densities of the two strongest RPA states in the 640-keV energy bins centered at $E_x$ = 10.3, 14.1 and 22.5 MeV, respectively. The corresponding collective model transition densities were built upon the $EL$ strengths given by the MDA of 240 MeV data [7]. The quoted percentages are the exhausted fractions of the isoscalar $EL$ EWSR.

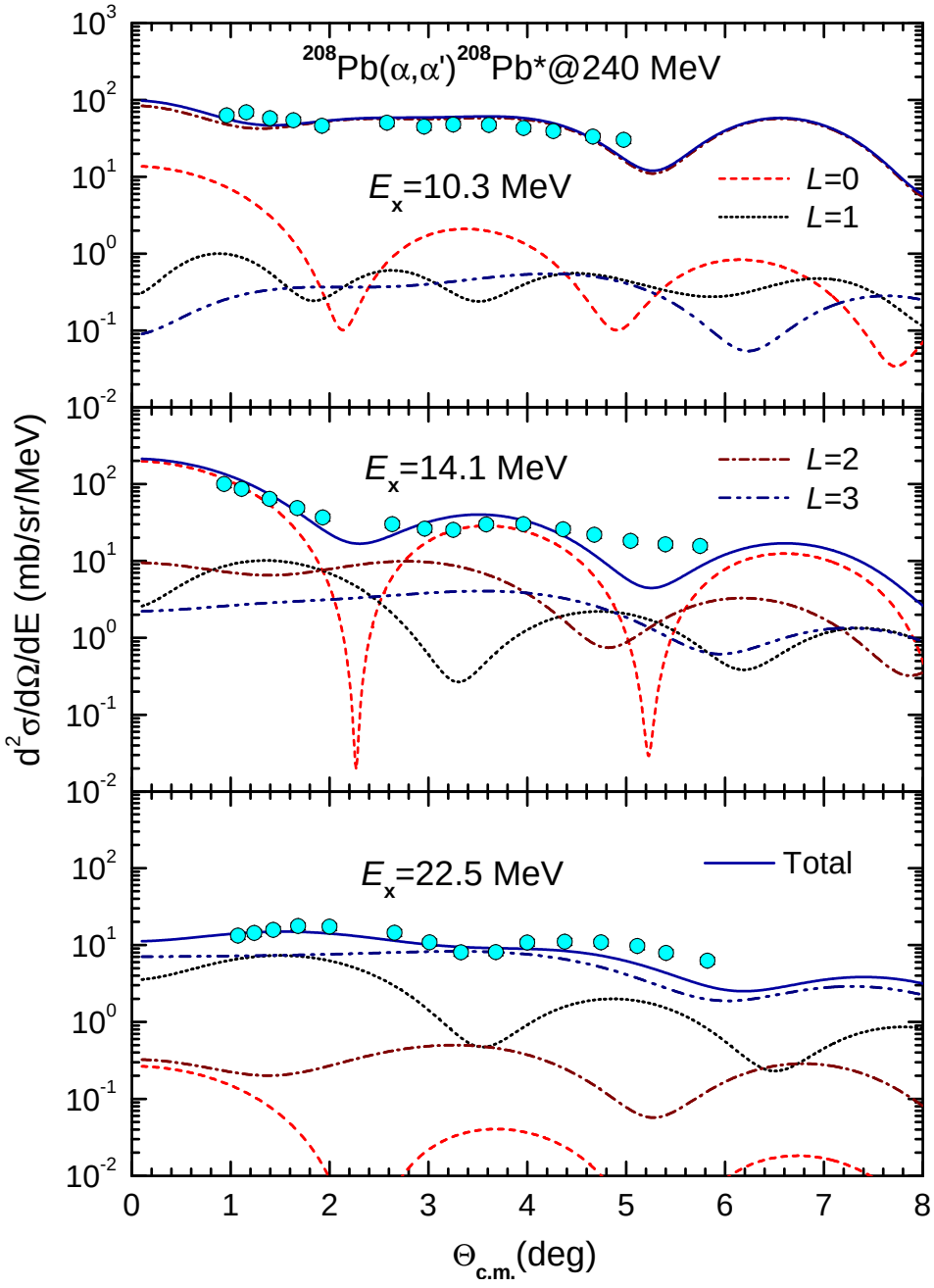


Figure 14: Inelastic $\alpha$+$^{208}$Pb scattering data at $E_{\rm lab}$ = 240 MeV measured for the 640 keV energy bins centered at $E_x$ = 10.3, 14.1 and 22.5 MeV respectively [7], in comparison with the DFM + DWBA results obtained with the total RPA transition densities (23) which give the fractions of the isoscalar $EL$ EWSR shown in Table 3.

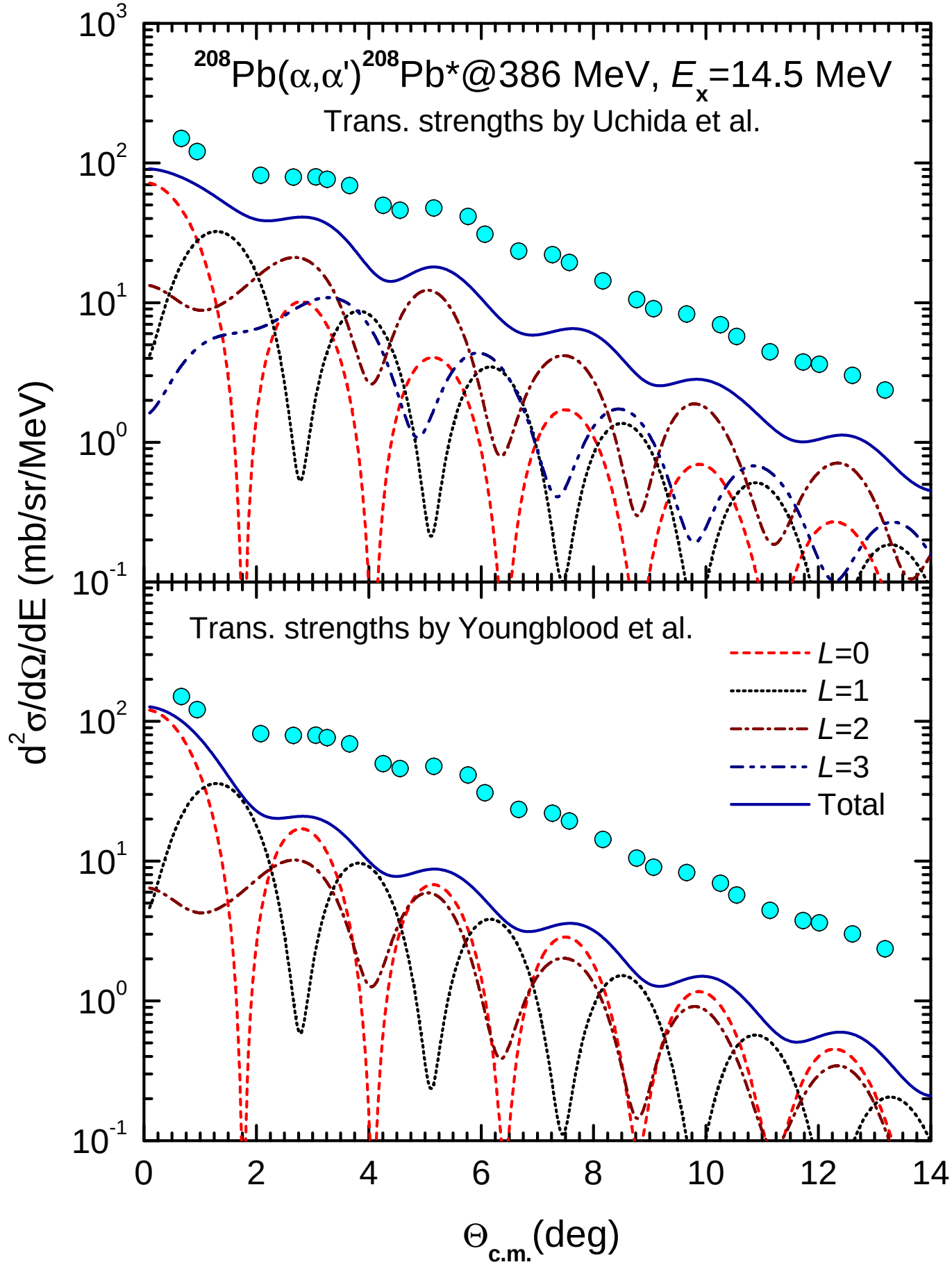
$^{208}$Pb(α,α')$^{208}$Pb*@386 MeV, $E_x$=14.5 MeV
Trans. strengths by Uchida et al.
Trans. strengths by Youngblood et al.
L=0
L=1
L=2
L=3
Total
d$^2$σ/dΩ/dE (mb/sr/MeV)
Θ$_{c.m.}$(deg)
10$^3$
10$^2$
10$^1$
10$^0$
10$^{-1}$
0
2
4
6
8
10
12
14